

**AFRL-SN-RS-TR-1998-120**

**In-House Report**

**July 1998**



# **SIMULTANEOUS TIME, WAVELENGTH AND INTENSITY MEASUREMENT OF OPTICAL MEMORY SUBSYSTEMS**

**Joseph Osman and Rebecca Bussjager**

**Sponsored by  
Ballistic Missile Defense Organization**

*APPROVED FOR PUBLIC RELEASE; DISTRIBUTION UNLIMITED*

The views and conclusions contained in this document are those of the authors and should not be interpreted as necessarily representing the official policies, either expressed or implied, of the Ballistic Missile Defense Organization or the U.S. Government.

**AIR FORCE RESEARCH LABORATORY  
SENSORS DIRECTORATE  
ROME RESEARCH SITE  
ROME, NEW YORK**

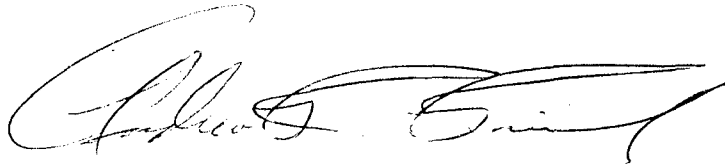
19980911 000

**DECLASSIFIED BY 7-11-2000**

This report has been reviewed by the Air Force Research Laboratory, Information Directorate, Public Affairs Office (IFOIPA) and is releasable to the National Technical Information Service (NTIS). At NTIS it will be releasable to the general public, including foreign nations.

AFRL-SN-RS-TR-1998-120 has been reviewed and is approved for publication.

APPROVED:



ANDREW R. PIRICH  
Chief, Photonics Processing Branch  
Sensors Directorate

FOR THE DIRECTOR:



ROBERT G. POLCE  
Acting Chief, Rome Operations Office  
Sensors Directorate

If your address has changed or if you wish to be removed from the Air Force Research Laboratory Rome Research Site mailing list, or if the addressee is no longer employed by your organization, please notify AFRL/SNDP, 25 Electronic Pky, Rome, NY 13441-4515. This will assist us in maintaining a current mailing list.

Do not return copies of this report unless contractual obligations or notices on a specific document require that it be returned.

REPORT DOCUMENTATION PAGE			Form Approved OMB No. 0704-0188	
<small>Public reporting burden for this collection of information is estimated to average 1 hour per response, including the time for reviewing instructions, searching existing data sources, gathering and maintaining the data needed, and completing and reviewing the collection of information. Send comments regarding this burden estimate or any other aspect of this collection of information, including suggestions for reducing this burden, to Washington Headquarters Services, Directorate for Information Operations and Reports, 1215 Jefferson Davis Highway, Suite 1204, Arlington, VA 22202-4302, and to the Office of Management and Budget, Paperwork Reduction Project (0704-0188), Washington, DC 20503.</small>				
1. AGENCY USE ONLY (Leave blank)		2. REPORT DATE July 1998		3. REPORT TYPE AND DATES COVERED In-House, Mar 96 - Mar 97
4. TITLE AND SUBTITLE  SIMULTANEOUS TIME, WAVELENGTH AND INTENSITY MEASUREMENT OF OPTICAL MEMORY SUBSYSTEMS			5. FUNDING NUMBERS PE - 61102F PR - 2300 TA - 06 WU -03	
6. AUTHOR(S)  Joseph Osman and Rebecca Bussjager				
7. PERFORMING ORGANIZATION NAME(S) AND ADDRESS(ES)  AFRL/SNDP 25 Electronic Pky Rome, NY 13441-4515			8. PERFORMING ORGANIZATION REPORT NUMBER  AFRL-SN-RS-TR-1998-120	
9. SPONSORING/MONITORING AGENCY NAME(S) AND ADDRESS(ES)  Ballistic Missile Defense Organization      AFRL/SNDP 7100 Defense Pentagon                              25 Electronic Pky Wash DC 20301-7100                              Rome, NY 13441-4515			10. SPONSORING/MONITORING AGENCY REPORT NUMBER  AFRL-SN-RS-TR-1998-120	
11. SUPPLEMENTARY NOTES  Air Force Research Laboratory Project Engineer: Joseph Osman/SNDP/(315)330-7671.				
12a. DISTRIBUTION AVAILABILITY STATEMENT  APPROVED FOR PUBLIC RELEASE; DISTRIBUTION UNLIMITED.			12b. DISTRIBUTION CODE	
13. ABSTRACT (Maximum 200 words)  This study showed that in WO <sub>3</sub> , there are plenty of defect states available to undergo transitions at 532 nm. We may have to read at a different wavelength further away from the bandgap of WO <sub>3</sub> (350 nm). We proved that the 1.06 um is acting mostly as heat, not as a transition source. We found it may be possible to work the system at the power density level of 650 uW/um <sup>2</sup> (532 nm) and 520 uWum <sup>2</sup> (1.06 um). Although the worst case of our Raman noise experiments showed a 19% standard deviation, this is still a much better signal to noise ratio than any current optical recording read. Our Raman spot size study, in cooperation with STM studies at Bates College, showed: a) the distribution of Raman scattering centers on the surface of common WO <sub>3</sub> is spatially uniform, b) the density of defects scales as the square of the lateral extent of the observed region as does the topographical surface area and, c) at the power densities employed and the amount of oxygen substoichiometry employed, there appears to be little cooperativity between the chemistry occurring at different defect centers.				
14. SUBJECT TERMS  optical storage, optical memory, tungsten oxide, defects, Raman scattering			15. NUMBER OF PAGES 68	
			16. PRICE CODE	
17. SECURITY CLASSIFICATION OF REPORT  UNCLASSIFIED	18. SECURITY CLASSIFICATION OF THIS PAGE  UNCLASSIFIED	19. SECURITY CLASSIFICATION OF ABSTRACT  UNCLASSIFIED	20. LIMITATION OF ABSTRACT  UL	

# Table of Contents

<b>1. INTRODUCTION</b>	1
<b>2. THEORY</b>	3
2.1 BACKGROUND	3
2.2 STRUCTURE OF $\text{WO}_3$ AND $\text{M}_x\text{WO}_3$	3
2.3 SHEAR PLANES IN SUBSTOICHIOMETRIC $\text{WO}_3$	4
2.4 THE BAND STRUCTURE	5
<b>3. EXPERIMENTS</b>	7
3.1 RATE CONSTANTS-532 NM ONLY	7
3.1.1 Introduction	7
3.1.2 Experimental	8
3.1.3 Results & Discussion	9
3.1.3.1 532 only 0 to 110 mW 180 ps pulses 400 msec exposure.	9
3.1.3.2 Complete turnover of woxyfoil material using 532 nm only.	11
3.1.3.3 Closer look at first deviation from linear increase.	13
3.1.3.4 Constant 532 nm only, varied accumulation time.	13
3.1.4 Conclusion	14
3.2 1.06 $\mu\text{m}$ RAMP MEASUREMENTS WITH CONSTANT 532 NM.	14
3.2.1 Introduction	14
3.2.2 Experimental	15
3.2.3 Results & Discussion	15
3.2.3.1 Increased 1.06 $\mu\text{m}$ with 532 nm kept constant at 8 mW.	15
3.2.4 Conclusions	18
3.3 532 NM RAMP WITH 1.06 $\mu\text{m}$ FIXED MEASUREMENTS.	18
3.3.1 Introduction	18
3.3.2 Experimental	18
3.3.3 Results & Discussions	18
3.3.3.1 Kept 1.06 $\mu\text{m}$ constant at 20 mW and varied 532 nm.	18
3.3.3.2 Looked more closely at first deviation from linear increase.	19
3.3.4 Conclusions	20
3.4 RAMAN NOISE MEASUREMENTS.	20
3.4.1 Introduction	20
3.4.2 Experimental	20
3.4.3 Results & Discussion	20
3.4.3.1 6.85 mW Raman Noise Results	20
3.4.3.2 21 mW Raman Noise Results	22
3.4.4 Conclusions	22
3.5 SPOT SIZE	22
3.5.1 Introduction	22
3.5.2 Experimental.	23
3.5.3 Results	23
3.5.3.1 Spiricon results	23
3.5.3.2 Photon results-Raman vs. Incident power at constant power density.	24
3.5.4 Discussion	25

## Table of Contents

3.5.5 <i>Conclusions</i> .....	26
<b>4. CONCLUSION</b> .....	26
4.1 THESE EXPERIMENTS .....	26
4.2 FURTHER EXPERIMENTS .....	27
4.3 PAYOFF .....	27
<b>APPENDIX A. A SURFACE RAMAN AND SCANNING TUNNELING MICROSCOPY STUDY OF THE SPATIAL DISTRIBUTION OF CORNER-SHARING AND EDGE-SHARING OCTAHEDRA ON THERMALLY OXIDIZED TUNGSTEN</b> .....	A1
<b>APPENDIX B. A SURFACE RAMAN-SCANNING TUNNELING MICROSCOPY STUDY OF THE SPATIAL DISTRIBUTION OF CORNER-SHARING AND EDGE-SHARING OCTAHEDRA ON THERMALLY OXIDIZED TUNGSTEN</b> .....	B1

# Table of Figures

Figure 1. System Schematic. . . . .	1
Figure 2. Filled circles are $W^{6+}$ , open circles are $O^{2-}$ , MI is a metal ion. . . . .	3
Figure 3. $WO_3$ structure. . . . .	3
Figure 4. $MO_6$ octahedra stacking . . . . .	3
Figure 5. Antiphase boundary (on left) and crystallographic shear (on right) along 2 different crystallographic directions. . . . .	4
Figure 6. A {001} shear plane in $WO_3$ . Shaded areas are $WO_6$ octahedra as viewed from above . . . . .	4
Figure 7. Idealized structure of $W_2O_5$ ( $WO_{2.5}$ ). . . . .	5
Figure 8. $W_{18}O_{49}$ ( $WO_{2.72}$ ). . . . .	5
Figure 9. Ionic-model of the band gap in $MgO$ . . . . .	6
Figure 10. MO Diagram and DOS for $WO_3$ . . . . .	6
Figure 11. Optical absorption vs. wavelength for 3 crystals varying in W/O ratio. . . . .	7
Figure 12. Experimental Setup. . . . .	8
Figure 13. Typical Raman Spectrum. . . . .	9
Figure 14. 532 only 0 to 110 mW 180 ps pulses 400 msec exposure. . . . .	10
Figure 15. Complete turnover of woxyfoil material using 532 nm only. . . . .	11
Figure 16. log log plot of data in Figure 15 with dark counts subtracted. . . . .	11
Figure 17. log C vs. log P . . . . .	12
Figure 18. B to C break revisited. . . . .	13
Figure 19. Long time scale accumulation 34 mW. . . . .	13
Figure 20. Long time scale accumulation 27 mW. . . . .	14
Figure 21. Increased 1.06 $\mu m$ with 532 nm kept constant at 8 mW. . . . .	15
Figure 22. Temperature from linewidth (Fazio Nash data) . . . . .	16
Figure 23. Temperature of material at each incident power . . . . .	16
Figure 24. Arrhenius plot . . . . .	17
Figure 25. Power Index. . . . .	17
Figure 26. 532 Ramp with 1.06 $\mu m$ constant. . . . .	18
Figure 27. log log plot of Figure 26 data. . . . .	19
Figure 28. Second look at first dip in Figure 26 data. . . . .	19
Figure 29. Raman Noise Measurement. . . . .	20
Figure 30. Histogram and Gaussian Curve Fit. . . . .	21
Figure 31. Raman Noise Measurement. . . . .	21
Figure 32. Raman Noise Measurement . . . . .	22
Figure 33. Power density using Spiricon. . . . .	23
Figure 34. 2/25/97 data . . . . .	24
Figure 35. Quadratic Fit. . . . .	24

## 1. Introduction

Systems requirements for projected future AF radar and intelligence signal processing systems include large capacity, high speed memory storage. The use of optics provides both speed and density advantages over electronic approaches. Optical transitions can be very fast, and the massively parallel nature of optical systems can provide for high throughput information storage.

Photonics Center scientists and engineers are working to replace current optical storage technology with parallel channel read/write heads and photochromic optical media. This photochromic optical memory system, co-invented by Rome Laboratory and Syracuse University, is based on transition metal oxide thin films. These films change color and electrical resistance when written by light of the proper wavelengths and beam size. Data stored on these optical disks can be read using changes in reflectance, electrical resistance or Raman scattering. Written spots are permanent until erased with infrared light that is powerful enough to heat the spot to over 380° C. The disk can be written using blue or ultraviolet fiber laser bundles or laser arrays allowing an entire sector to be written or read at once. Data from many sources can be simultaneously written and needed data can be read by a separate parallel channel read head.

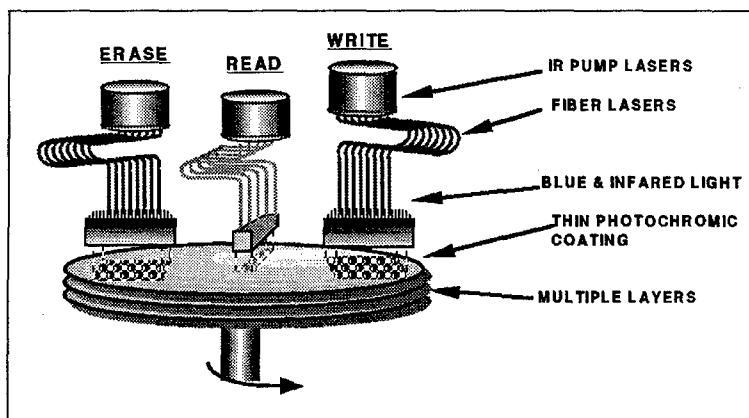


Figure 1. System Schematic.

Our current system has a better signal to noise ratio, faster access time, lower power consumption and improved data density compared to magneto-optic (MO) or phase change systems with single read/write heads. The current technology leader is phase change, which has problem of "bit creep" limiting density. MO is capable of higher density, but is expensive due to low manufacturing yields and has adhesion problems (drop outs). All removable high density magnetic systems require lasers for tracking, necessitating a dual magnetic and optical system.

The parallel nature of our system can solve the current bottleneck in transferring data from processors to memory. This bottleneck is being experienced by Air Force systems that manage massive amounts of information from multiple sources. The Air Force deficiency we are initially addressing is parallel storage and read out of events during exercises for ACC. The new memory system will also correct deficiencies identified in the Air Force Mission Support System (AFMSS), the Airborne Warning and Control System (AWACS), the Distributed Air Operations Center (DAOC) and the Joint STARS System. Civilian multimedia technology will be improved

by efficiently synchronizing video and audio output while the computer is simultaneously processing user input.

This thin film memory was the result of a joint Syracuse University-Rome Laboratory effort that resulted in a patent application. The key to our patent was our discovery that 532 nm and 1060 nm light, when spatially overlapped on tungsten oxide powder, would cause a permanent yellow  $\text{WO}_3$  to blue  $\text{W}_2\text{O}_5$  color change in ambient atmospheric conditions. We deduced that the 1060 nm light was heating the lattice, and allowing the material to restructure into the  $\text{W}_2\text{O}_5$  blue form before it cooled. We reasoned that by using the 1060 nm light alone, we would be able to erase the material. We tested our theory, and the material erased completely. We also determined that heating the material above about 400 C for a few seconds in an oven would perform a global erase.

Our initial discovery of the effect was on loose powder, so our first priority was on producing usable forms of the material, capable of reproducible results and fixed micron size sites for repeatability and extended time studies. We have developed two forms of the material. The first we call Woxyfoil™, which consists of tungsten foil carefully oxidized on the surface only. The other is thin films of tungsten oxide deposited on quartz substrates. We used the Raman spectroscopy setup in laboratory 21 to characterize these materials as we developed them.

The object of this project was to perform optical power threshold experiments to determine how much light is needed to effect the yellow to green transition. We rebuilt our system to include more precise spot size measurement capability and to shorten the optical path lengths in the system to keep the beams as small and free of aberrations as possible. We had already determined that we would be able to make both forms of material we have developed so far undergo transition by either the blue-green wavelength or the IR wavelength alone.

We wanted to measure the temporal pulse response, wavelength dependency and readout intensity of our new optical memory. These would give a detailed view of energy and mass transfer rates in the material. The kinetics of heating, transition and cooling occur too quickly to measure by ordinary chemical means. We would then use these measurements to model the interaction between the two wavelengths, to determine the charge transfer mechanism that the blue green wavelength uses to change the material color, as well as prove that the fixing of the material color change is due to the heating effect of the infrared wavelength.

The Air Force requirement for dense storage memory systems will be met as quickly as possible by an early exploitation of the new discovery for disk memory systems. Successful completion of this and following efforts will lead to faster, more stable, erasable, ultra-dense optical memory systems for DoD mission planners, pilots needing mission maps and threat databases, intelligence data storage, and for command and control, radar data manipulation and battlefield management. In the civilian world, data storage is a very large multibillion dollar market. If we can begin strong commercial licensing and development, the timeline could be 2-3 years for a civilian medical storage system, and 3-4 years for an Air Force system.

Follow on systems may include multiple layer systems, consisting of other transition metal oxides in separate layers, and an ultradense single layer system that is currently in the patent disclosure stage. According to Dr. Mansuripur of the University of Arizona, author of "The Physical Principles of Magneto-Optical Recording", we are the only viable candidate for more than two layers of memory, because we have the ability to make each individual layer spectrally



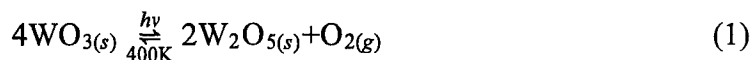
selective in its absorption. This we can do by individually doping each layer for absorption of a specific wavelength.

Because these materials change electrical resistance when they change colors, they can be used to make an optically addressable electronic memory capable of reading an entire page of optical data from a 3D optical memory or an entire optical memory card. The Air Force can use this initially in compact medical and maintenance records storage.

## 2. Theory

### 2.1 Background

Simultaneously presented YAG laser beams at 1.06 microns and (doubled YAG) at 532 nanometers were used to write bits on the film. The 532 nanometer radiation causes a fast electron transfer which is manifested in a yellow to blue color shift. The shift is made permanent by the heating effect of the 1.06 micron beam (milliseconds) which drives out bonded oxygen. This is the chemical reaction



which is permanent until the material is reheated to a temperature greater than 400° C. Bits are read in less than one microsecond using the direct reflection or the Raman emission of the 532 nanometer laser used alone. Erase is accomplished using the 1.06 micron beam alone.

### 2.2 Structure of $\text{WO}_3$ and $\text{M}_x\text{WO}_3$

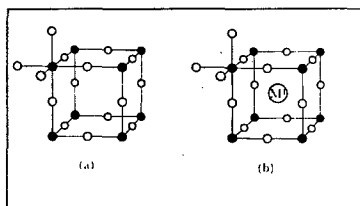


**Figure 2.** Filled circles are  $\text{W}^{6+}$ , open circles are  $\text{O}^{2-}$ ,  $\text{M}^+$  is a metal ion<sup>1</sup>.

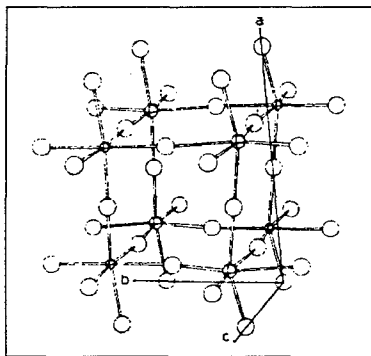


**Figure 3.**  $\text{WO}_3$  structure<sup>2</sup>.

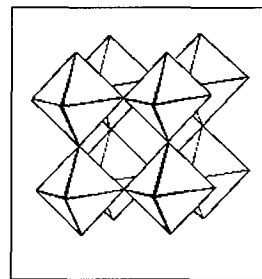


**Figure 4.**  $\text{MO}_6$  octahedra stacking<sup>3</sup>

$\text{WO}_3$  has a distorted version of the  $\text{ReO}_3$  structure (figure 2a), which is a simple cubic lattice of tungsten with each tungsten atom the center of a  $\text{WO}_6$  octahedron. Figure 3 shows a more accurate representation of the  $\text{WO}_3$  structure. When small amounts of metals (M), usually protons from hydrogen or sodium metal, are added to  $\text{WO}_3$ , a tungsten bronze  $\text{M}_x\text{WO}_3$  is formed. The  $\text{WO}_3$  lattice restructures with a proton or a positive metal ion in the center of the simple cubic tungsten lattice (figure 2b), and the material turns blue. In tungsten bronzes, metal atoms donate their electrons to the empty conduction band of the host  $\text{WO}_3$  lattice. These extra

electrons lead to a semiconducting or a metallic state, depending on  $x$ . The octahedra stacking is shown in Figure 4. Notice that in  $\text{WO}_3$ , the octahedra share corners only.

### 2.3 Shear Planes in Substoichiometric $\text{WO}_3$

When  $\text{WO}_3$  is heated in vacuum, oxygen and water are driven off, and the material becomes substoichiometric  $\text{WO}_{3-x}$  with  $x$  being a small number.

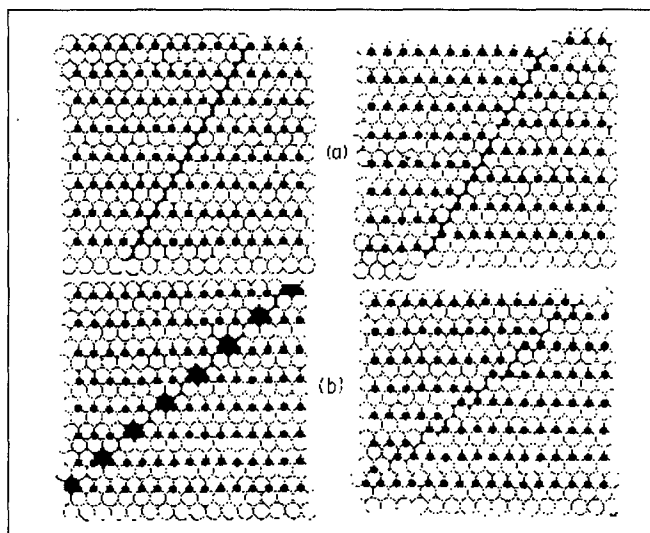


**Figure 5.** Antiphase boundary (on left) and crystallographic shear (on right) along 2 different crystallographic directions<sup>4</sup>.

As illustrated in Figure 5, when the material is being heated, oxygen vacancies preferentially form discs and then planes. These planes are called antiphase boundaries. When there is enough energy in the lattice, the lattice shears along the plane of vacancies, removing the vacancies. This is called crystallographic shear. In  $\text{WO}_3$ , the  $\text{WO}_6$  octahedra share corners before shearing, as is shown in figure 4. After shearing, some or all neighboring octahedra along the CS plane share edges, as shown in figure 6. This results in removing some oxygen atoms.

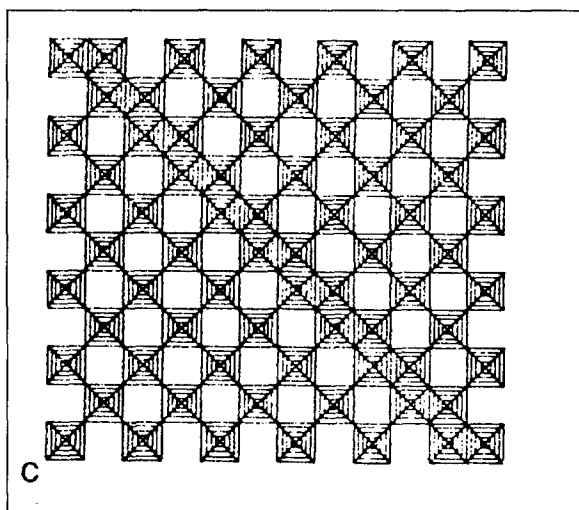


**Figure 6.** A  $\{001\}$  shear plane in  $\text{WO}_3$ . Shaded areas are  $\text{WO}_6$  octahedra as viewed from above<sup>5</sup>.

Crystallographic Shear (CS) or Magnelli phases are quasistable. In  $\text{WO}_3$  they initially are of the form  $\text{M}_n\text{O}_{3n-1}$ , and occur along the  $\{102\}$  crystallographic direction. These range from  $\text{W}_{25}\text{O}_{74}$  ( $\text{WO}_{2.96}$ ) to  $\text{W}_{15}\text{O}_{44}$  ( $\text{WO}_{2.933}$ ). Further reduction causes the CS planes to occur along the  $\{103\}$  crystallographic direction, and create phases of the form  $\text{M}_n\text{O}_{3n-2}$ . These include  $\text{W}_{50}\text{O}_{148}$  ( $\text{WO}_{2.96}$ ),  $\text{W}_{40}\text{O}_{118}$  ( $\text{WO}_{2.95}$ ) and  $\text{W}_{20}\text{O}_{58}$  ( $\text{WO}_{2.90}$ ). In addition,  $\{001\}$  shear planes have been reported<sup>6</sup>.

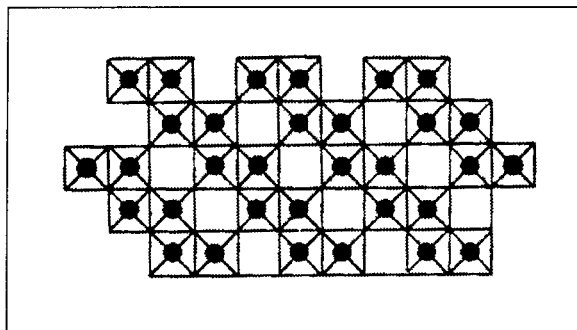


**Figure 7.** Idealized structure of  $\text{W}_2\text{O}_5$  ( $\text{WO}_{2.5}$ )<sup>6</sup>.

The theoretical form of  $\text{W}_2\text{O}_5$  ( $\text{WO}_{2.5}$ ) is shown in Figure 7. There is also a unique extremely stable phase that forms readily under a wide range of conditions when  $\text{WO}_3$  is reduced. This is  $\text{W}_{18}\text{O}_{49}$  ( $\text{WO}_{2.72}$ ), as shown in Figure 8.

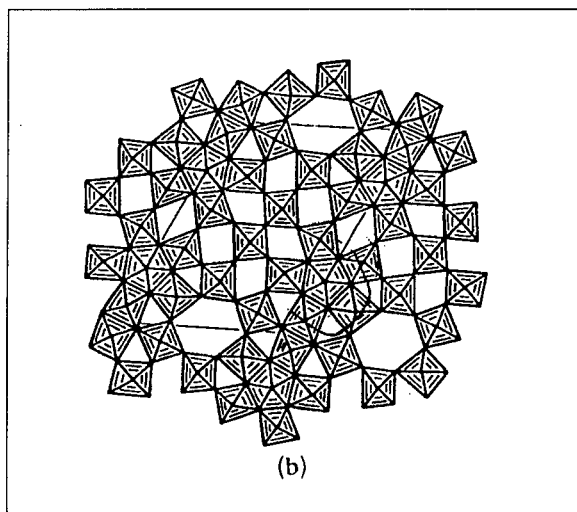


**Figure 8.**  $\text{W}_{18}\text{O}_{49}$  ( $\text{WO}_{2.72}$ )<sup>7</sup>.

## 2.4 The Band Structure

In  $\text{WO}_3$ , the  $\text{Mg}^+/\text{Mg}^{2+}$  of Figure 9 is replaced mostly by  $\text{W}^{6+}(5d)$  orbitals. The Madelung potential is an electrostatic potential acting on an electron due to the ionicity of the lattice. The polarization is the polarization the electron causes in the nearby lattice. The overlap is the broadening of electronic levels due to the spatial overlap between ions.

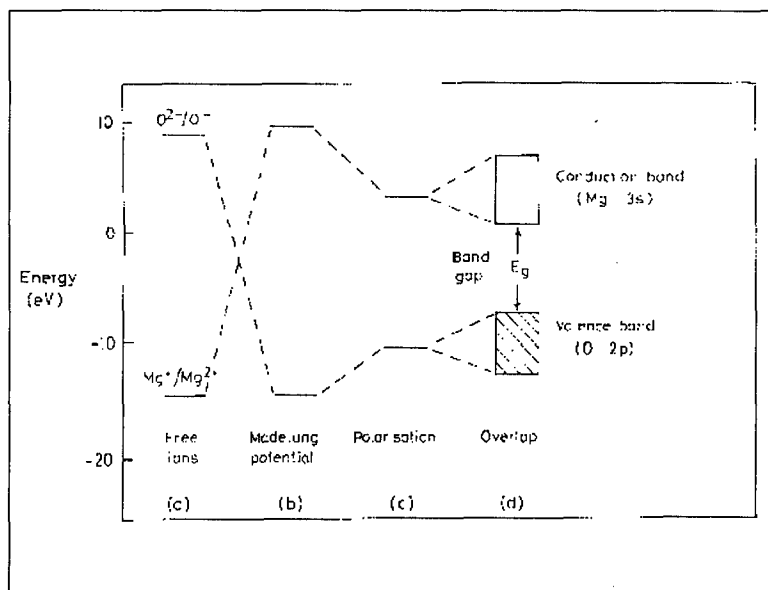


Figure 9. Ionic-model of the band gap in  $MgO$  <sup>8</sup>.

$WO_3$  is more complex than the simple picture of Figure 9 for  $MgO$ . In  $WO_3$ , since the  $O^{2-}(2p)$  orbitals are lower in energy than the  $W^{6+}(5d)$  orbitals, the empty valence band is formed from a bonding combination of the  $O^{2-}(2p)$  orbitals and mostly the  $W^{6+}(5d)$  orbital. Similarly, the conduction band is formed from an antibonding combination of the  $O^{2-}(2p)$  orbitals and mostly the  $W^{6+}(5d)$  orbital.

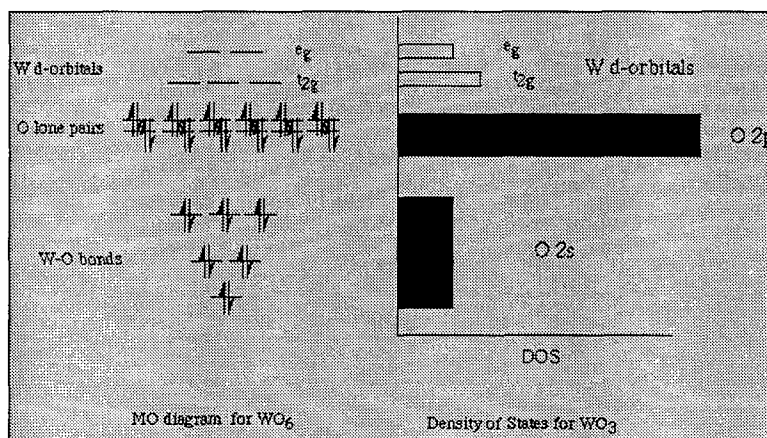


Figure 10. MO Diagram and DOS for  $WO_3$  <sup>9</sup>.

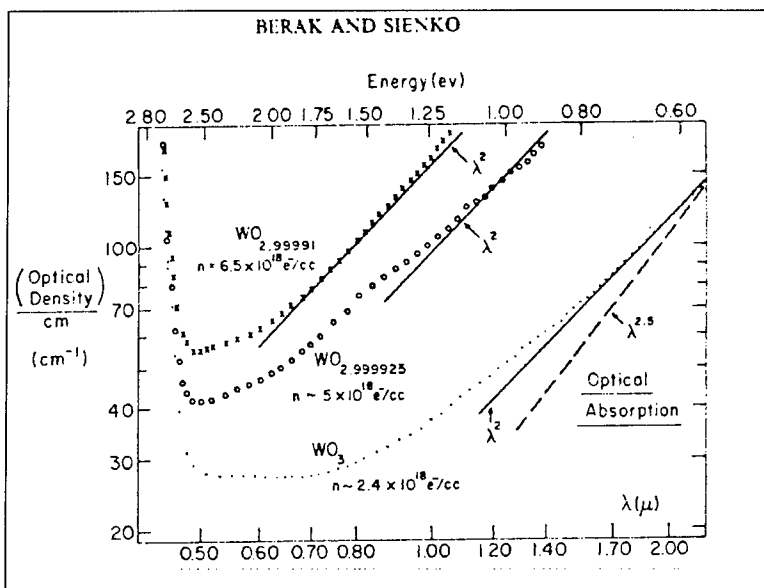


Figure 11. Optical absorption vs. wavelength for 3 crystals varying in W/O ratio<sup>10</sup>.

The band gap,  $E_g$ , is about 2.7 eV for  $WO_3$ . This is a small energy compared to the much larger effects shown in Figure 9. The band gap can not yet be accurately calculated from the spectroscopic levels, then applying the Madelung potential and so on. It must be measured, as it was for Figure 11, which shows the allowed transition of electrons from the top of the filled band to the bottom of the empty band.

Although  $WO_3$  has a small semiconductor-like band gap, many other transition metal oxides end up with a wider gap, and thus are insulators, or have overlap between the valence and conduction bands, and thus are metallic.

### 3. Experiments

#### 3.1 Rate Constants-532 nm only

##### 3.1.1 Introduction

The purpose of our setup was to allow us to measure absolute rate constants under conditions of constant collision frequency with the surrounding air. The collision frequency is determined by the partial pressure of oxygen in the air, which was assumed to be constant.

We then used our spot size measurement capability to determine the optical power per unit area needed to cause the transition. Dr. Chaiken of Syracuse University and his students performed much the same experiment measuring temperature instead of optical power. Their apparatus allowed control of the collision frequency of oxygen with the material, while ours allowed precise measurements of laser power per unit area. These parallel experiments gave us the upper and lower bounds on the transition energy.

### 3.1.2 Experimental

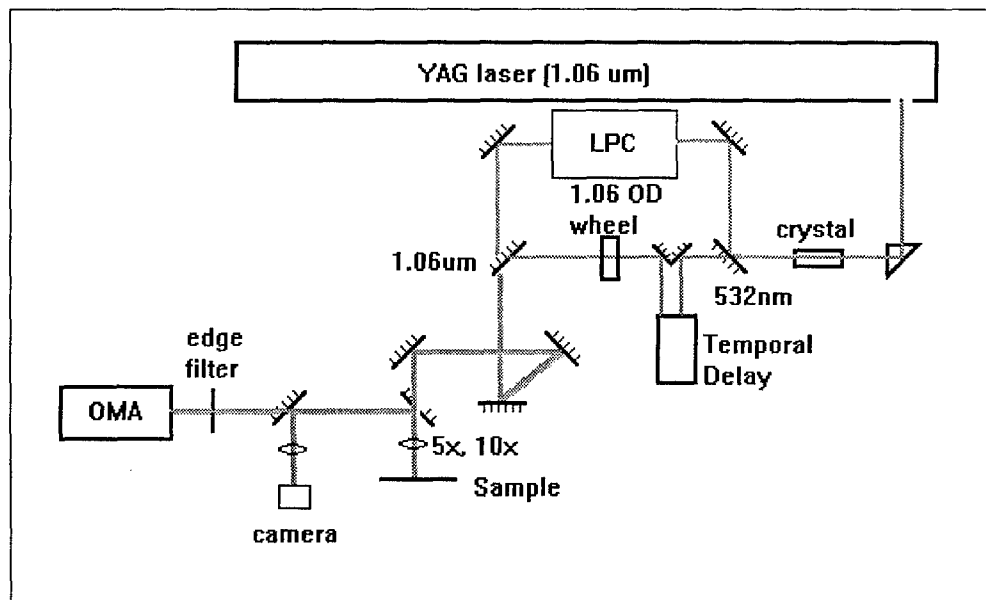


Figure 12. Experimental Setup.

150 ps pulses from a mode locked Q-switched Quantronix Model 4116 Nd:YAG laser were frequency doubled using a Quantronix Model 324 SHG frequency doubler. The non-doubled 1.06  $\mu\text{m}$  and the doubled 532 nm light were coaxial on exit from the doubler and were separated by the next 2 mirrors, which were harmonic separators, specially coated for this purpose. The separated beams were amplitude controlled by either a CRI Model LPC-VIS laser power controller (LPC) or a circular variable OD filter. If both wavelengths were needed, they were combined in a 532 nm reflective mirror. The coaxial beams were sent through a 5x or 10x microscope objective. The small spot was incident normally to the sample, and some of the reflected light as well as the Raman scattered light were directed to the optical multichannel analyzer (OMA). Some light was split off using a beamsplitter into a Pulnix Model TM-540 CCD camera.

The pulse duration was measured using an Antel AR-G20 detector and a Tektronix sampling oscilloscope system consisting of an S-4 sampling head, a 7S11 sampling sweep unit, a 7T11A sampling time base and a 7104 mainframe. The Q-switched PRF was 5.00 kHz. The average power was 4.1 W as measured by a Coherent LabMaster with M45 detector. The Q-switched pulse envelope allowed 10 pulses through each time it was open, which at 5.00 kHz was every 200 ms.

The OMA gives a plot of counts vs. channel number, or when calibrated, counts vs. wavelength. Figure 13 shows a typical result. The highlighted area in the largest peak is the integration interval whose integrated total counts are saved as the data for each run. These totals are then plotted after all the runs for that experiment are completed, as shown in Figure 14 and following plots.

The OMA does not start counting photons immediately. There is a 16 ms dead time at the beginning of the OMA accumulation. As there is more power to convert  $\text{WO}_3$  to  $\text{W}_2\text{O}_5$ , more material is being converted in the dead time, and the total count rate decreases.

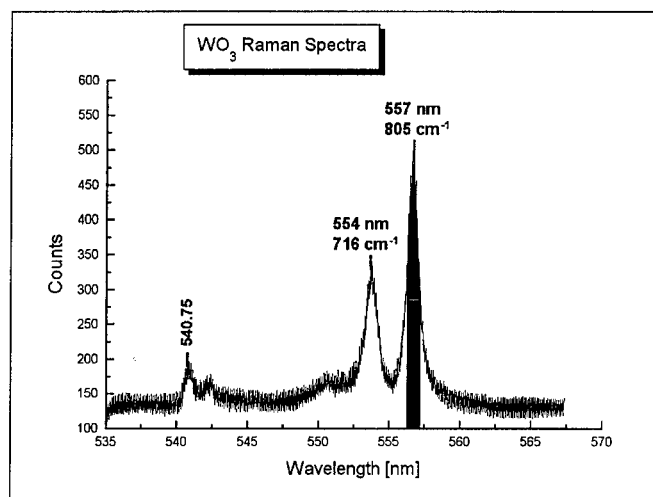


Figure 13. Typical Raman Spectrum.

The shape of the Raman peaks gives information about the type of transition process involved. Inhomogeneous processes occur when the local environment of the oscillators involved in the transition changes individually. In  $\text{WO}_3$ , for instance, defects may preferentially move closer to either the oxygen or the tungsten upon irradiation. Inhomogeneous processes and instrumental broadening have a Gaussian line shape. Homogeneous processes have a Lorentzian line shape.

### 3.1.3 Results & Discussion

#### 3.1.3.1 532 only 0 to 110 mW 180 ps pulses 400 msec exposure.

The initial experiment was to determine the low power threshold of 532 nm light alone that would cause color change due to self heating as well as the high power threshold of 532 nm alone that would saturate the color change.

The rate  $r$  for a one photon process is proportional to the photon flux density, that is the number of photons incident on the material per unit time. This can be expressed as  $r_1 \propto I/h\nu$ , where  $I$  is the irradiance (intensity) in  $\text{W/m}^2$  and  $h\nu$  is the energy of a single photon. For a 2 photon process  $r_s \propto r_1(I/h\nu)$  and in general  $r_n \propto r_{n-1}(I/h\nu)$ . Taking the log of both sides gives  $\log r_n = n \log(I/h\nu)$  and the slope of the log log plot of incident power vs. integrated counts gives us a power index  $n$  for the process involved. So, for example, a two photon process would have a power index of 2. Raman scattering of our material is a one photon process. As you increase the incident light intensity, you increase the number of photons to be scattered. There is a study<sup>11</sup> showing that the volume increase with a Gaussian laser beam on streaming gas goes as the  $3/2$  power. As the penetration depth increases, more Raman scatterers are excited at depth, but they are less likely to contribute to the overall Raman signal, because there are less of them, and they are absorbed and scattered out more. The upper bound in power for Raman and volume together is  $5/2$  or 2.5.

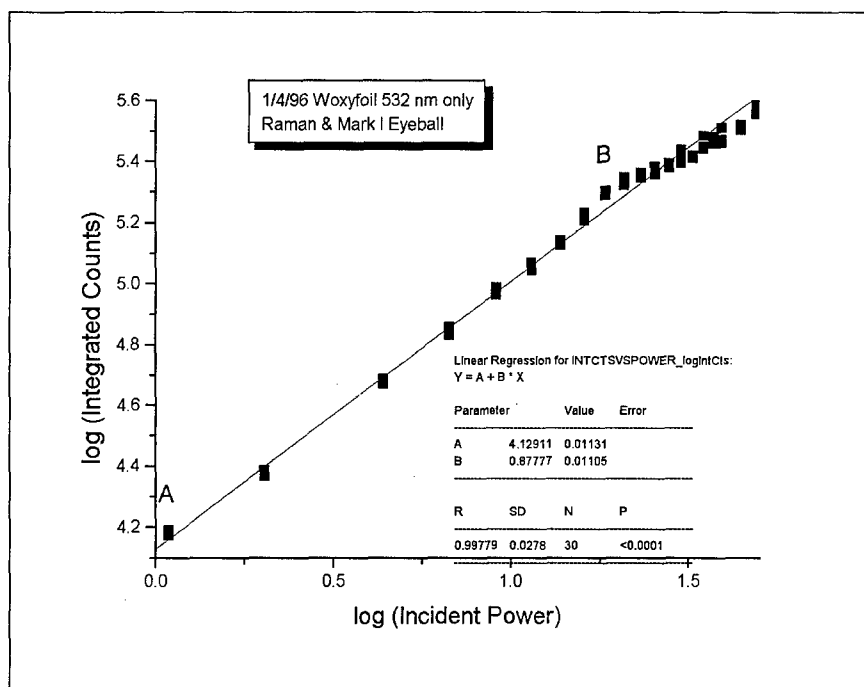


Figure 14. 532 only 0 to 110 mW 180 ps pulses 400 msec exposure.

From A to B we had a power index of 0.87. The difference from 2.5 in the power index shows that one or more other processes are occurring other than just increasing Raman scatterers and volume in the material. Most probably, even if we don't see written material until point B, material is being converted from the Raman scattering yellow state to the blue state at all times after the start of the plot, point A, thus decreasing the power index. If we assume that this is the only additional process occurring, we can fix the upper bound in its power at  $2.5 - 0.87 = 1.63$ . Oxides in general have plenty of defects, and in  $\text{WO}_3$ , there are plenty of defect states available to undergo transitions at 532 nm. This shows that there may be no lower limit for the read beam, if the read beam is 532 nm. We may have to read at a different wavelength further away from the bandgap of  $\text{WO}_3$ , which is about 350 nm.

By visual inspection, we found the lower threshold for a written spot to be 23 mW average power (point B) into a 4  $\mu\text{m}$  diameter spot. This corresponds to  $1.83 \text{ mW}/\mu\text{m}^2$  average power density. Since the modelocked Q-switched pulse envelope allowed ten 180 ps pulses through each time it was open, which at 5.00 kHz was every 200  $\mu\text{s}$ , the duty cycle was  $9 \times 10^{-6}$ , and the peak power threshold was  $(1/\text{duty cycle}) \times 1.83 \text{ mW} = 203 \text{ W}/\mu\text{m}^2$ . This then is the lower limit for a 532 nm write beam, if the system works on reflectance contrast, and is as good as the human eye.

We could not saturate the color change with the maximum available power of 53 mW on the sample (100 mW at the LPC). We then completely realigned the laser system to finally produce at least 400 mW at the LPC. This higher power required a slightly smaller aperture to keep a nice  $\text{TEM}_{00}$  mode. These apertures were made by the RL machine shop.



### 3.1.3.2 Complete turnover of woxyfoil material using 532 nm only.

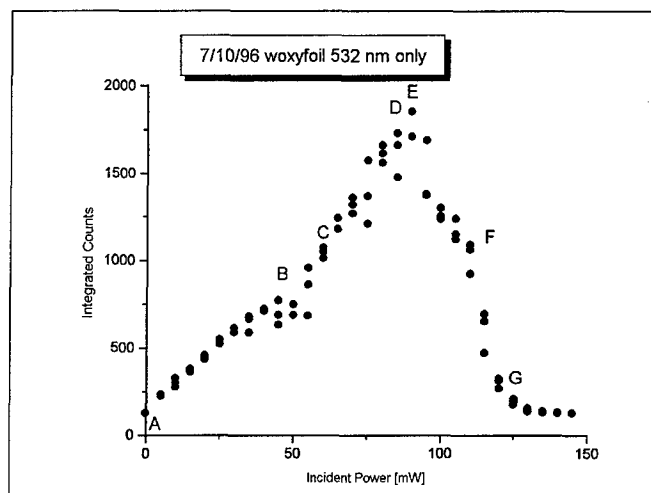


Figure 15. Complete turnover of woxyfoil material using 532 nm only.

The initial increase is due to the increase in Raman scatterers due to the increased light flux. The decline in counts after the turnover point (E) is most probably due to the fact that the material conversion during the initial 16 ms dead time of the detector is greater than the increase in counts due to the increased photons to be scattered. It could also be due to laser ablation decreasing the depth of oxide material past the penetration depth. At the point G, all the octahedra have been converted in the detector deadtime.

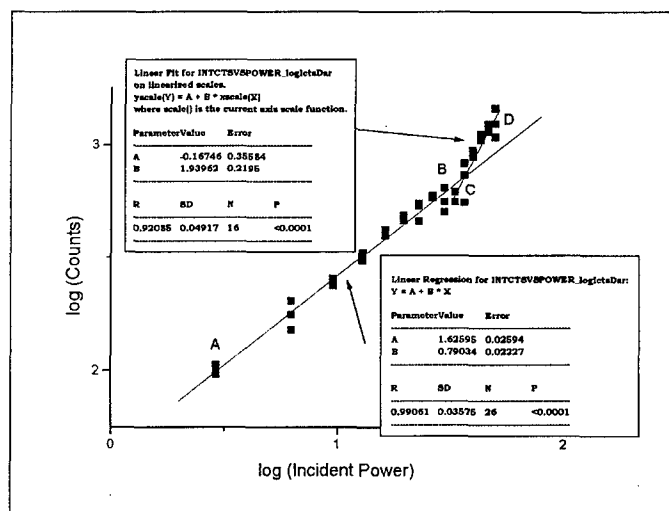


Figure 16. log log plot of data in Figure 15 with dark counts subtracted.

The exposure time for this experiment is 1 second.

From A to B we had a power index of 0.79. As before, if we assume that this is the only additional process occurring, we can fix the upper bound in its power at  $2.5 - 0.79 = 1.71$ .

The break from B to C may be due to reaching a threshold for water desorption/evaporation and/or penetration to a more metallic layer in the center of the foil.

The power index from C to D is 1.94. The upper bound for processes other than Raman and volume increase is then  $2.5 - 1.94 = 0.55$ . The decrease may be due to a beam diameter increase with no penetration depth increase. Then the increase in scatterers would scale as the area, rather than as a volume. This would occur if the light penetration reached a more metallic layer in the center or lacking such a layer, the other side of the woxyfoil. It could also be due to laser ablation of the material with each 180 ps pulse removing material converted by the previous pulse.

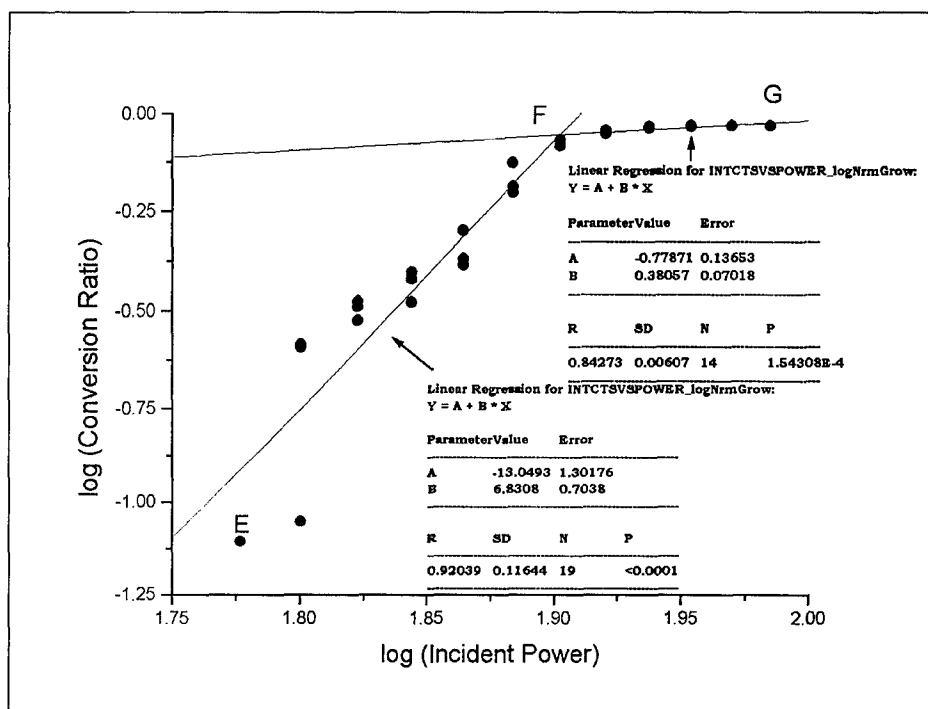


Figure 17.  $\log C$  vs.  $\log P$

In order to more directly show the rate of yellow to blue conversion after the turnover point, we took all points including and after the turnover point, subtracted the dark current, and normalized the values to an average peak value of 1. This gave a relative normalized non converted (yellow) to converted (blue and everything else that does not produce Raman scatterers) ratio. Subtracting this from 1 gave the relative normalized conversion ratio  $C$ . The power index,

$$N = \frac{\log C}{\log P} \quad (2)$$

where  $P$  is the power, is an increasing function whose slope of 7.1 from points E to F indicates that a many photon process is occurring.

### 3.1.3.3 Closer look at first deviation from linear increase.

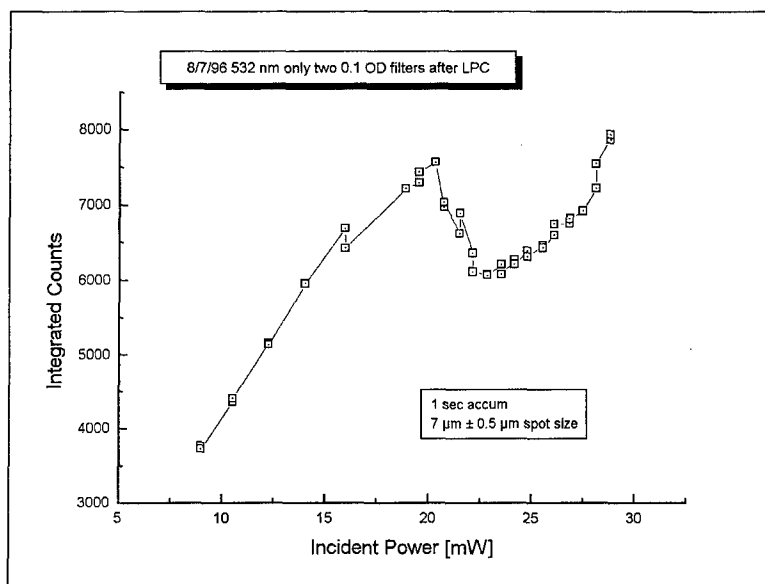


Figure 18. B to C break revisited.

In order to rule out any chance that the oxidized foil had a bad spot, we reran the portion of the experiment (from B to C in Figure 15), and proved that this is a real effect. Note the difference in the break location on the X axis. We may have had poor repeatability in the peak position from one area of the foil to another.

We should rerun this with wet and dry (baked) foils to determine if the cause of the break is a threshold for water desorption/evaporation. To determine if penetration to a more metallic layer in the center of the foil is the cause we should use foils with obvious metal center layers, as well as pressed powder samples, which have no metallic center.

### 3.1.3.4 Constant 532 nm only, varied accumulation time.

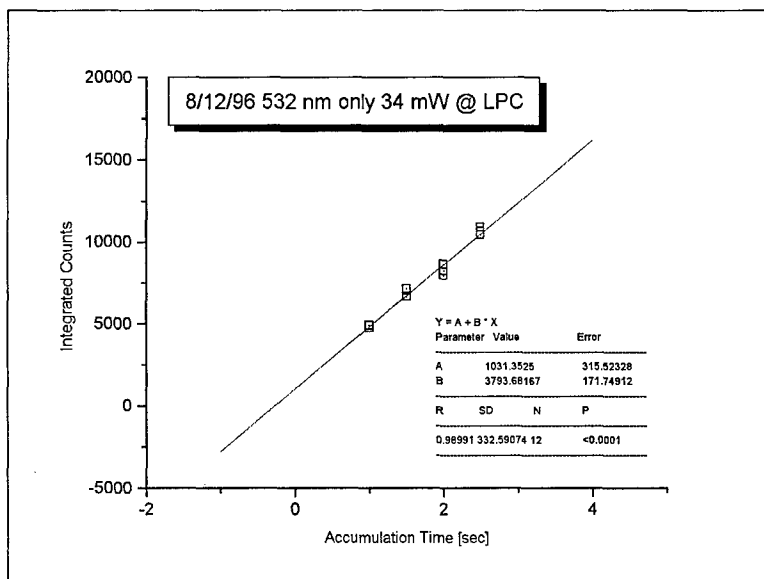


Figure 19. Long time scale accumulation 34 mW.

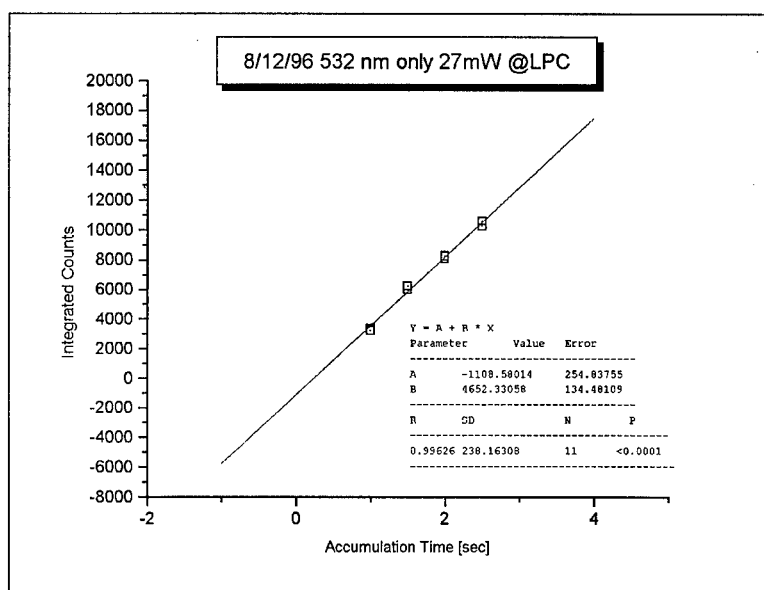


Figure 20. Long time scale accumulation 27 mW.

The linear nature of these plots shows that there is no chemistry going on after 1 second (5,000 pulses). The linear nature of the scale shows that the only effect occurring is increase in scattered photons due to the increase in time.

### 3.1.4 Conclusion

Oxides in general have plenty of defects. The wide range of power indices at different incident power ranges in these experiments show the complicated nature of oxides. In  $\text{WO}_3$ , there are plenty of defect states available to undergo transitions at 532 nm. This experiment shows that there may be no lower limit for the read beam, if the read beam is 532 nm. We may have to read at a different wavelength further away from the bandgap of  $\text{WO}_3$ , which is approximately 350 nm.

## 3.2 1.06 $\mu\text{m}$ Ramp Measurements with Constant 532 nm.

### 3.2.1 Introduction

The line width of the Raman spectrum can give information about the temperature and the lifetime of the transition.

The principal process involved in line broadening is the homogeneous process of lifetime broadening. When the Schrodinger equation is solved for a system that is changing with time, the energy levels can not be specified exactly in the solution. If the average time the system survives is the lifetime  $\tau$ , then its energy levels are blurred to an extent of order  $\delta E$ , where  $\delta E \approx \hbar/\tau$ . The uncertainty of the wavelength  $\delta\lambda$  is related to  $\delta E$  by  $E = (\hbar c/\lambda)$ . The line width  $\delta\tilde{\nu}$  is related to the energy spread by  $\delta E = \hbar c(\delta\tilde{\nu})$ . The practical form of this is  $\delta\tilde{\nu} = (5.32\text{cm}^{-1})/(\tau/\text{ps})$ . The rate constant  $k$  is inversely proportional to  $\tau$ , so the line width  $\delta\tilde{\nu}$  is directly proportional to the rate constant  $k$ .

Arrhenius relation

$$k = Ae^{-E^*/RT} \text{ or } \log_{10} k = \log_{10} A - \frac{E^*}{2.303RT} \quad (3)$$

is usually plotted as  $\log k$  vs.  $1/T$ . If this is a straight line then the process is an activated process, one which requires energy higher than a threshold, called the activation energy, to proceed. The slope of the  $\log k$  vs.  $1/T$  line is  $E_a/MK$  where  $E_a/M$  is the molar activation energy and  $K$  is Boltzmann's constant or  $E_a/R$ , where  $R$  is the gas constant. Studies by Nash and others at Syracuse University have shown that Raman response of  $WO_3$  to actual heating of the substrate by electrical heaters gives a linear activated process. Since the line width  $\delta\tilde{\nu}$  is directly proportional to the rate constant  $k$ , we plotted  $\log \delta\tilde{\nu}$  vs.  $1/P$  for our laser heating experiment.

### 3.2.2 Experimental

These experiments were performed as in Section 3.1.2, but with 1.06  $\mu\text{m}$  light being added to the system. All these measurements were with the 1.06  $\mu\text{m}$  pulse 1.2 ns before the 532 nm pulse. As far as we could tell, the 1.06  $\mu\text{m}$  spot size was larger than the 532 nm spot size. We always made sure they were coaxial before taking measurements.

### 3.2.3 Results & Discussion

#### 3.2.3.1 Increased 1.06 $\mu\text{m}$ with 532 nm kept constant at 8 mW.

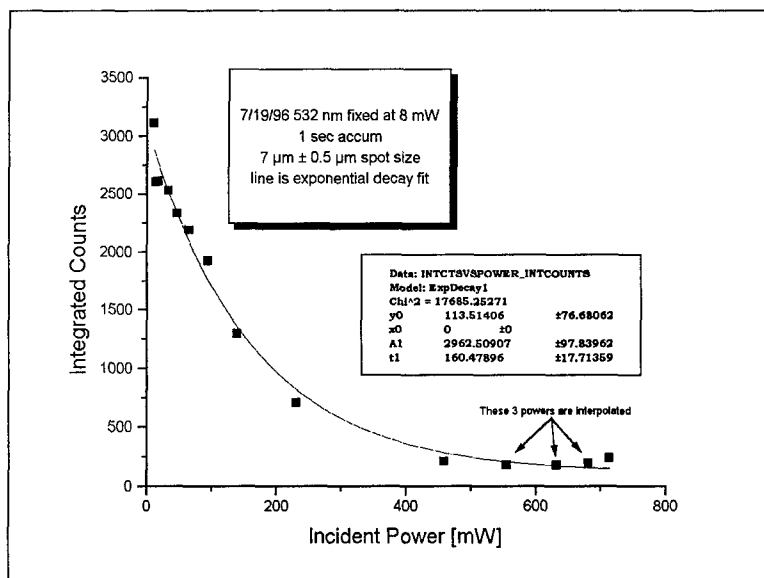


Figure 21. Increased 1.06  $\mu\text{m}$  with 532 nm kept constant at 8 mW.

The exponential fit of Figure 21 shows that it is Arrhenius like in its behaviour. This means that 1.06  $\mu\text{m}$  is acting mostly as heat, not as a transition source.

Fazio Nash of Syracuse University has taken data on  $WO_3$  that shows the dependence of line width on temperature. Using his results (Figure 22), we were able to determine the temperature of the material at the time the Raman photons were collected (figure 23). We can not get  $T$  from line widths when ramping 532 nm, as line width broadening due to higher 532 nm intensity is much greater than the lifetime broadening.

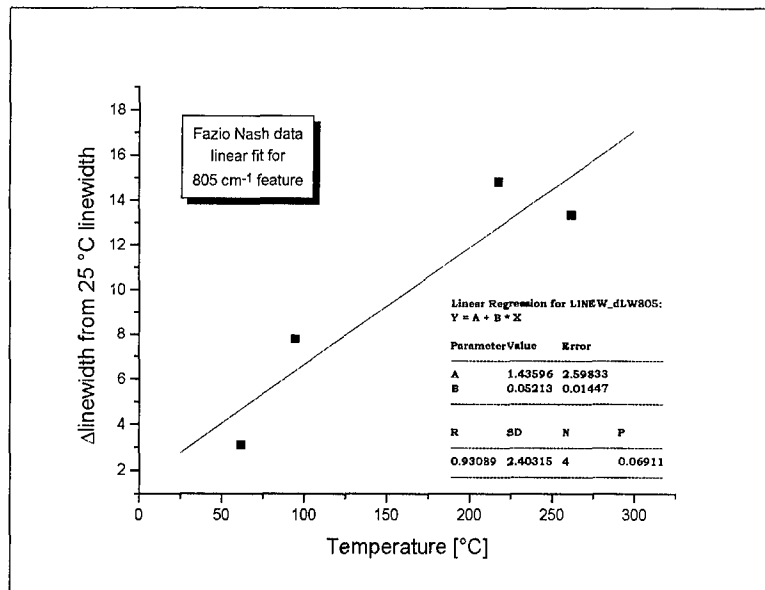


Figure 22. Temperature from linewidth (Fazio Nash data)

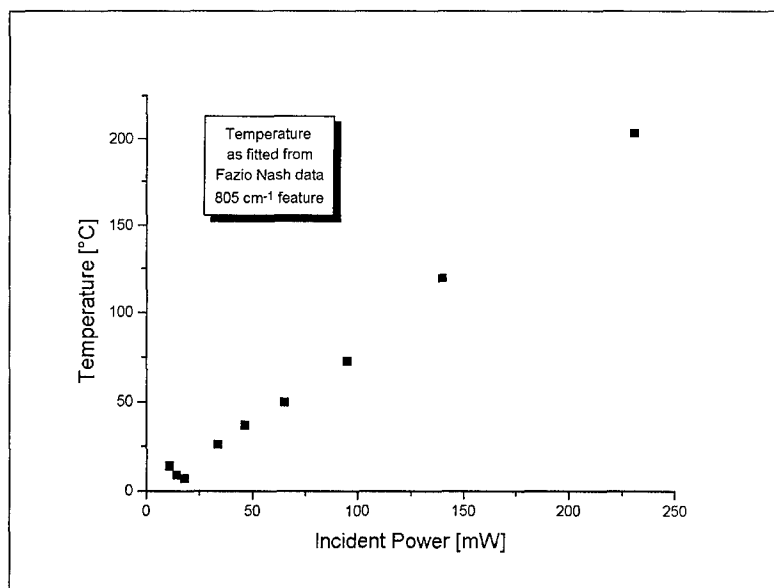


Figure 23. Temperature of material at each incident power

One explanation why the slope of Figure 23 is not one may be that the  $O_2$  atoms exiting the material take heat away from lattice as they leave. The Raman peaks we see are solely from corner sharing octahedra. We know from Winters' paper<sup>12</sup> that heating the material changes the  $O_2$  exchange rates of the material. As you heat up the medium, you desorb surface adsorbed gases, including oxygen. This changes the rate at which oxygen can leave the lattice itself, thus changing the rate at which octahedra reform to share edges. The Winters paper has thermal activation energies for oxygen exchange with the local atmosphere. Other papers may have surface mobility of oxygen changes.

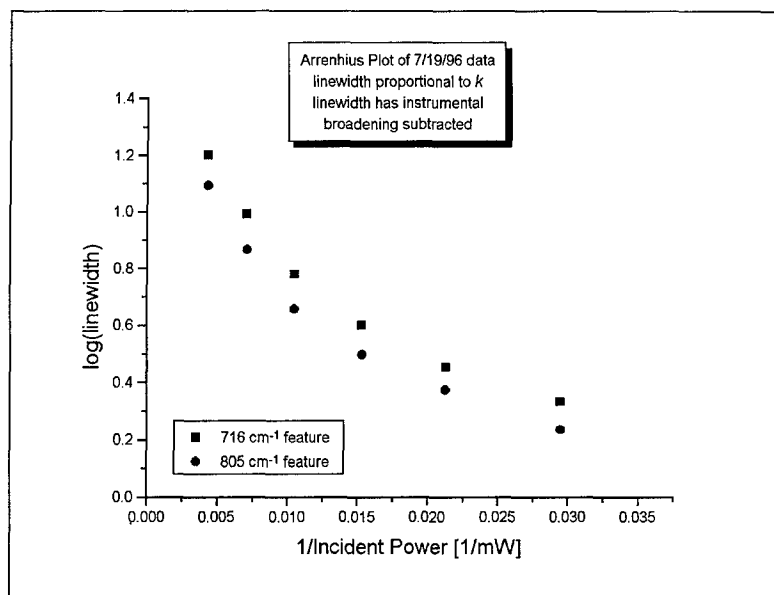


Figure 24. Arrhenius plot

The fact that Figure 24 is not linear indicates that the optical process is not straightforward random heating. We know that the material is absorptive at near IR wavelengths. We also used high peak power modelocked and Q-switched pulse trains. The combination of these two factors may have led to a nonlinear transformation and absorption process.

The relative normalized conversion ratio  $C$ , was determined as in Section 3.1.3.2. The power index was an increasing function whose slope of 0.5, which is less than 1, indicates that a single photon process was occurring.

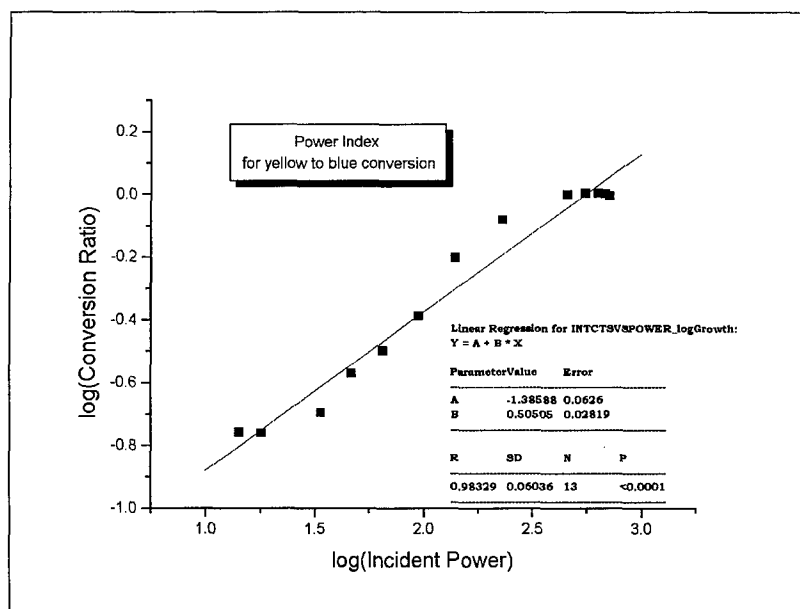


Figure 25. Power Index.

### 3.2.4 Conclusions

The exponential/logarithmic nature of Figure 21 means that  $1.06\ \mu\text{m}$  is acting mostly as heat, not as a transition source. Oxygen exchange with the atmosphere must be taken into account. As you heat up the medium, you desorb surface adsorbed gases, including oxygen. This changes the rate at which oxygen can leave the lattice itself, thus changing the rate at which octahedra reform to share edges. The fact that Figure 24 is not linear indicates that the optical process is not straightforward random heating. We know that the material is absorptive at near IR wavelengths. We also used high peak power modelocked and Q-switched pulse trains. The combination of these two factors may have led to a nonlinear transformation and absorption process.

### 3.3 532 nm Ramp With $1.06\ \mu\text{m}$ Fixed Measurements.

#### 3.3.1 Introduction

Having held the 532 nm power constant while ramping the  $1.06\ \mu\text{m}$  light, we also wanted to perform the reverse in order to further separate the transition contribution to change from the heating contribution.

#### 3.3.2 Experimental

These experiments were performed as in Section 3.2.2. The  $1.06\ \mu\text{m}$  power was controlled by a circularly variable OD wheel, which was carefully calibrated.

#### 3.3.3 Results & Discussions

##### 3.3.3.1 Kept $1.06\ \mu\text{m}$ constant at 20 mW and varied 532 nm.

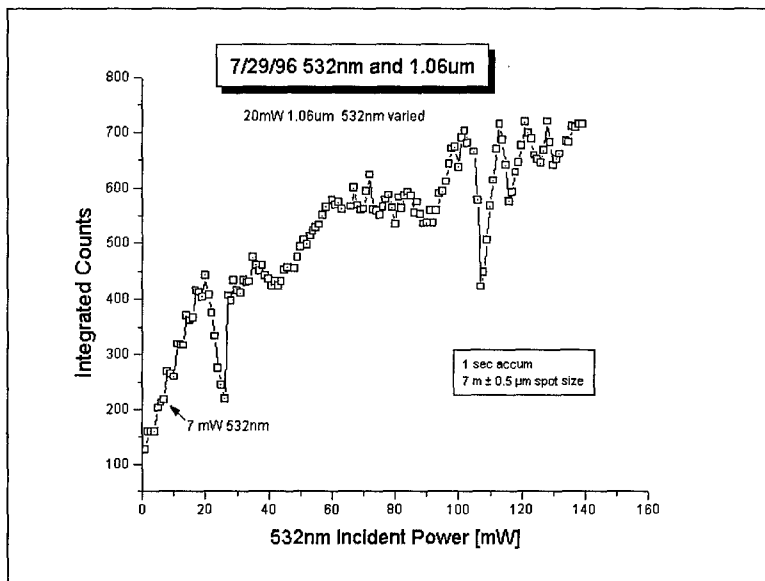


Figure 26. 532 Ramp with  $1.06\ \mu\text{m}$  constant.

It is interesting to note that we see a dip at the same location (20 mW 532 nm) as in the 532 nm only plot (Figure 15), but also that there is no turnover peak at 90 mW and no further drop to the baseline. The lack of turnover may be due to the IR keeping the lattice too warm to reconstruct into edge sharing octahedra.



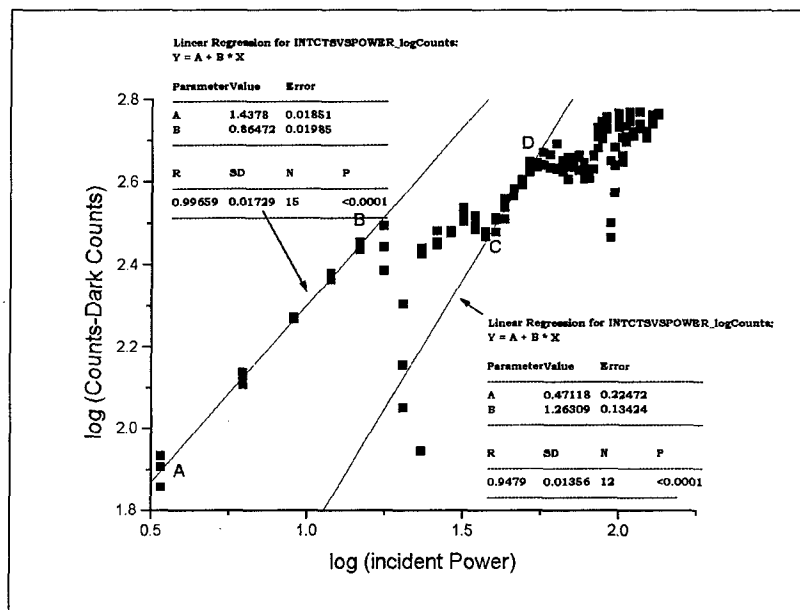


Figure 27. log log plot of Figure 26 data.

The slopes of the sections of the log log plot are similar to the 532 nm only case: 0.86 for the initial section, which compares with 0.79 and 0.87 for the 532 nm only plot, and 1.26 for the second section, which compares with 1.77 in the 532 nm only plot. The small added amount of 1.06  $\mu$ m light did not seem to affect the basic processes at lower powers of 532 nm light.

### 3.3.3.2 Looked more closely at first deviation from linear increase.

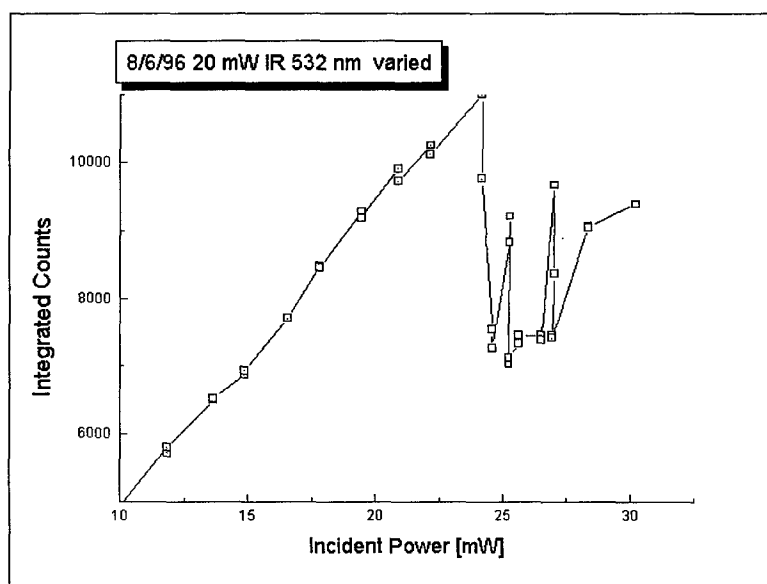


Figure 28. Second look at first dip in Figure 26 data.

Before taking this measurement, we added a delay line to the 1.06 beam line, and set the two beam distances to be equal so that the pulses were synchronous, and thus overlapped temporally.

This result was more irregular than the 532 nm only case. Since this dip is repeatable, we should see if it is enough variation to work the system at this power level. Our spot size was 7  $\mu\text{m}$  in diameter, which gives a power density for 532 nm light at 25 mW of  $650 \mu\text{W}/\mu\text{m}^2$ , and for 1.06  $\mu\text{m}$  light at 20 mW of  $520 \mu\text{W}/\mu\text{m}^2$ . This is significantly smaller than the powers needed for other optical media.

### 3.3.4 Conclusions

There is no turnover peak at 90 mW and no further drop to the baseline. The lack of turnover may be due to the IR keeping the lattice too warm to reconstruct into edge sharing octahedra. We should see if there is enough variation to work the system at the power density level for 532 nm light of  $650 \mu\text{W}/\mu\text{m}^2$ , and for 1.06  $\mu\text{m}$  light of  $520 \mu\text{W}/\mu\text{m}^2$ .

## 3.4 Raman noise measurements.

### 3.4.1 Introduction

Repeatability of peak and dip locations, as noted in previous sections of this report, had been a problem. Also we needed to find out the noise floor of our Raman read process. So we started with small power levels, such as we would use to read in a real system. We defined Raman noise as the deviation from linear response of Raman counts vs. position on the foil.

### 3.4.2 Experimental

These experiments were performed as in Section 3.1.2. As in all other experiments in this report, care was taken to ensure a flat defect free area was used for measurements.

### 3.4.3 Results & Discussion

#### 3.4.3.1 6.85 mW Raman Noise Results

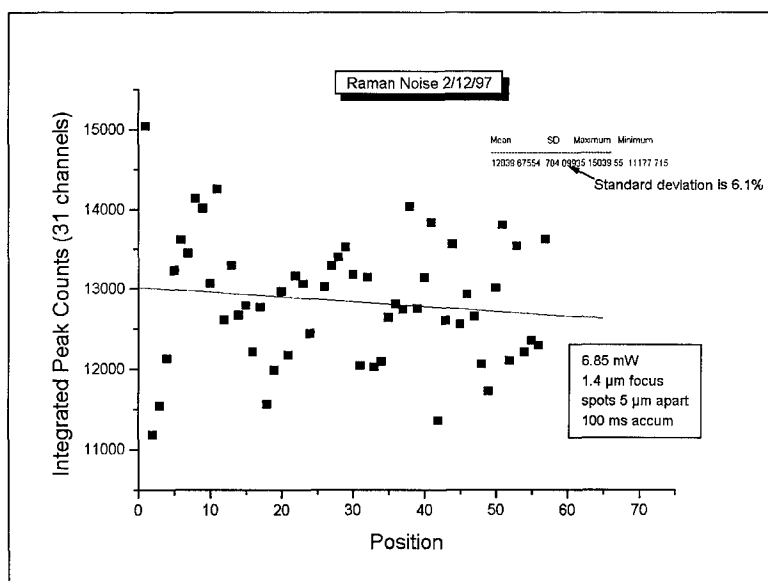


Figure 29. Raman Noise Measurement.

Position refers to position number. Each spot was at least 5 microns from any other. Some positions were farther apart, due either to experimental procedure glitches or reaching the edge of the foil. The standard deviation, and thus the Raman noise, was 6.1%.

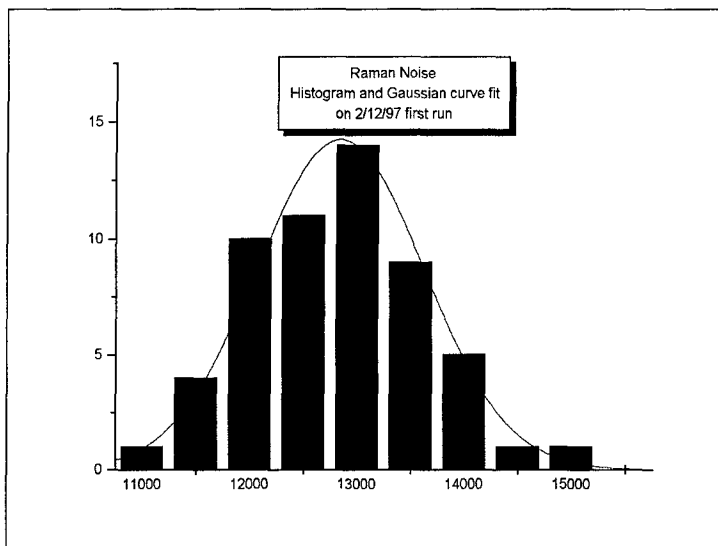


Figure 30. Histogram and Gaussian Curve Fit.

The closeness of fit to a Gaussian shows the random nature of readout noise.

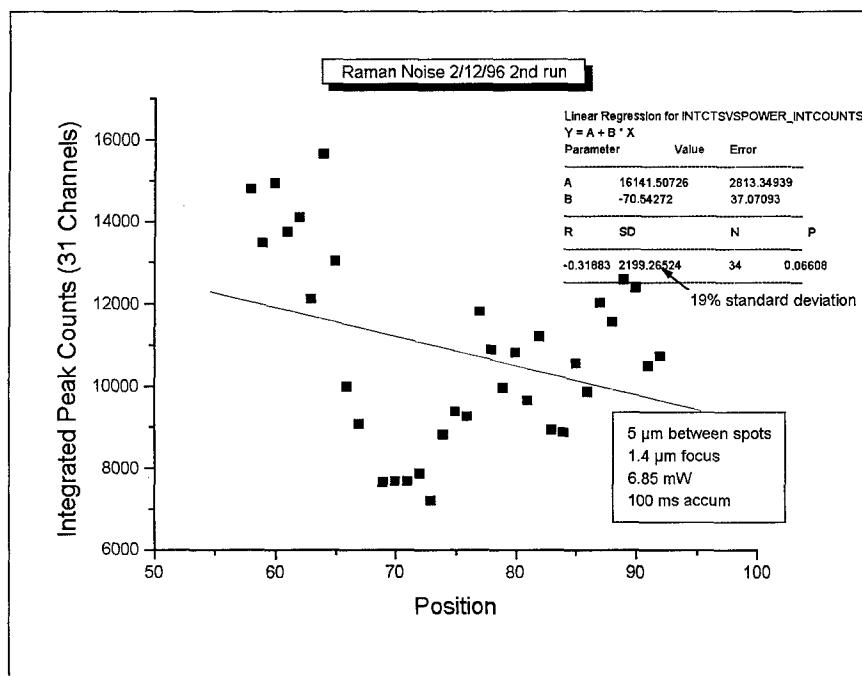


Figure 31. Raman Noise Measurement.

The apparent structure in these measurements could be due to a bowed foil. The standard deviation/Raman noise is 19%.

### 3.4.3.2 21 mW Raman Noise Results

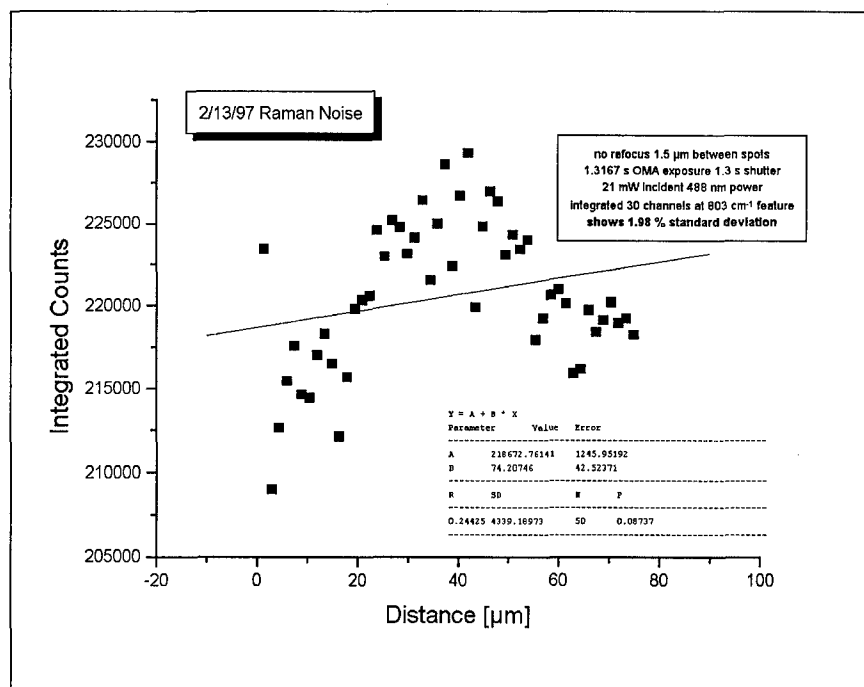


Figure 32. Raman Noise Measurement

We used a higher read power, and as we expected, the signal to noise ratio was better. The standard deviation/Raman noise improved to 1.98%.

### 3.4.4 Conclusions

Although one of our experiments showed a 19% standard deviation, this is still a much better read process, due to the zero signal on a written area, than any current optical recording system. For the purpose of these and coming experiments, every dip and peak should be redone on a different area to make sure it is repeatable, and thus real.

## 3.5 Spot Size

### 3.5.1 Introduction

We wanted to know if the spatial distribution of defect centers and the spatial distribution of scattering centers were complementary. We assumed that the entire surface is composed of only corner-sharing, Raman active octahedra or edge-sharing, Raman inactive octahedra. If the total Raman intensity scaled differently with increasing spot size than did the topographical area within the scanned region, then the spatial distribution of scattering centers was not uniform within the scattering volume. In addition to our Raman scattering intensity measurements, we used STM data from Matt Côté of Bates College to give a direct measure of topographical surface area on angstrom to micron spatial scales. The resulting papers are attached as Appendices A and B. The first will be published in "Chemical Aspects of Electronic Ceramics Processing", Proceedings of the Material Research Society, Vol. 495. The second has been submitted to Physical Review A. Given the complexity of oxide surfaces, particularly those in

contact with a crude ambient atmosphere, this comparison represents an unusual and possibly useful approach for characterizing the surfaces of metal oxides.

### 3.5.2 Experimental.

We started our spot size measurements using the Spiricon 2-d CCD system. In addition to the measurement system already described, optics and a camera were added so that it was possible to view the laser irradiated region from which Raman shifted photons were be collected. The plan was to make sure the spot was at its tightest focus on the material, then take 5 readings of the spot size image (about 1000  $\mu\text{m}$  in diameter) on the Spiricon. With the Spiricon, the spot image was elliptical and not always easily fit using a Gaussian profile. We moved the material for each reading. We knew from reticle measurements, as well as calculations using the NA of the microscope objective, that our smallest spot size was 1.4  $\mu\text{m}$ . Using our measured input power and the 1.4  $\mu\text{m}$  spot size, we calculated the power density of the readings. We then slightly defocused the spot, took 5 readings of the spot size image, determined the new spot size and calculated the new power necessary in order to keep the same power density as obtained when in focus. After adjusting the LPC to get as close to the target power as possible, we took 5 more measurements, again on a new spot each time.

### 3.5.3 Results

#### 3.5.3.1 Spiricon results

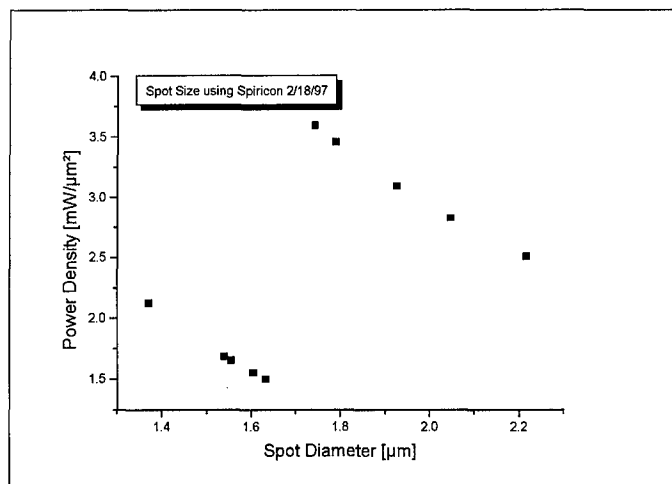


Figure 33. Power density using Spiricon.

As can be seen by Figure 33, we had a lot of trouble readjusting the Spiricon based system to keep a constant power density. We used the Spiricon for three other sets of data also. We did take over 60 Raman spectra, and it may be possible to use this data if we pick out the data that ends up having the same power density. As an example, using only the data having a power density between 0.09 and 0.10  $\text{mW}/\mu^2$  in Figure 34 we would have ten data points with a standard deviation of about 5%. Figure 34 shows about a 16% standard deviation in power density for all the data taken that day.

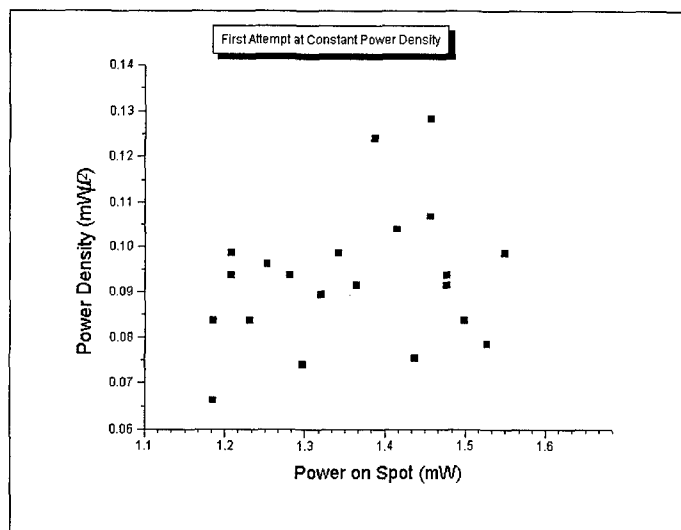


Figure 34. 2/25/97 data

### 3.5.3.2 Photon results-Raman vs. Incident power at constant power density.

Because of these problems, we began using the moving knife edge-based technique of the Photon Model 0390-STD/20390 Spot Scan instrument (Photon, Inc.). The small depth of focus employed in our experiments could be viewed directly on the active surface. This ensured that the focus size we measured using the Spot Scan was identical to the focus size that was employed in obtaining the Raman measurements of the  $W\text{O}_3$  surface. The spot shape was circular to visual examination and always easily fit using a Gaussian profile. The spot size for our purposes is defined arbitrarily as the 1/e point of the circularly symmetric spots. We were able to get about a 2.5% standard deviation using this system.

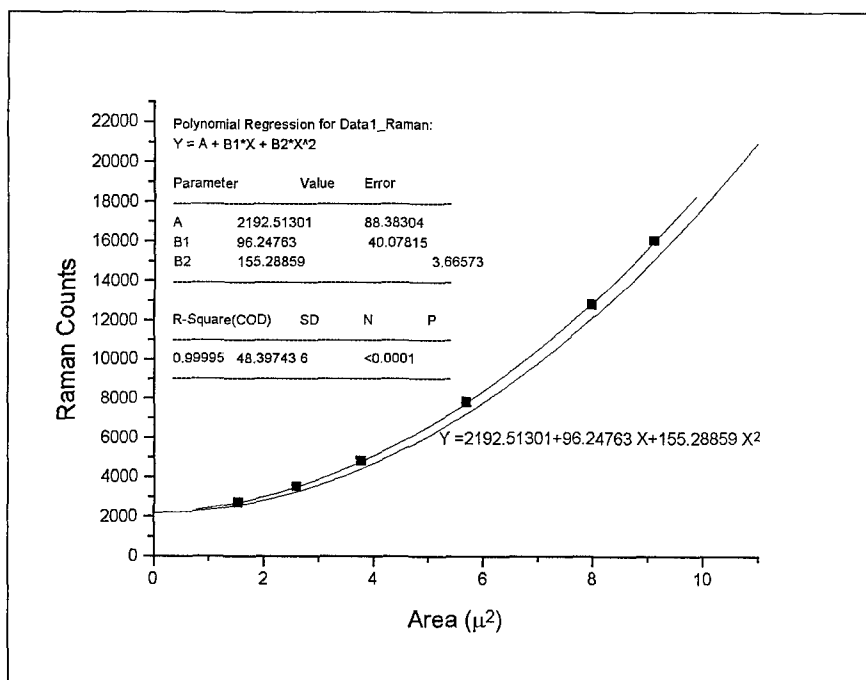


Figure 35. Quadratic Fit.

Figure 35 shows the dependence of the peak Raman signal at the  $805\text{ cm}^{-1}$  peak as a function of spot size for an essentially constant,  $1.91\text{ mW}/\mu\text{m}^2$ , power density. This figure clearly shows that the variation in Raman signal (the y axis), corresponding to a factor of three variation in spot area (the x axis), is accounted for in terms of a quadratic variation.

### 3.5.4 Discussion

We performed these Raman experiments at constant power density for two reasons. First, we wanted to have a constant penetration depth of the light into the oxide surface so that whatever variation in Raman strength was observed could be interpreted in terms of the increasing lateral extent of the exposed region. Second, from our earlier work, we knew that the degree of oxygen substoichiometry, as will be discussed below, would be a function of the applied power density. If the power density was not constant then the degree of substoichiometry would have varied. The Raman scattering and STM imaging results show that both the density of Raman scatterers and the topographical area vary as the square of the lateral extent of the region examined. The STM images (in Appendices A and B) define the surface of constant tunneling current indicated by the z coordinates. This would be expected if the Raman scattering centers were uniformly distributed across the oxide surface. Since we presume that the regions of edge sharing octahedra and corner sharing octahedra are complementary, this finding also suggests that the density of defects varies as if their spatial distribution were isotropic across the oxide surface.

The Raman experiments probed a region which is very large compared to the largest expected dimension of the CS planes so that we do not expect to be able to discern any structural features of individual CS planes. We assume that a large number always tended to be completely enveloped by the observation process. Since the Raman intensity varies quadratically with the spot size, we conclude that the spatial distribution of CS structures is uniform.

It should be noted that we have attempted to characterize the most common type of tungsten oxide one can prepare. Because of the inherent anisotropy or extremely small grain size of columnar amorphous evaporated films, either sputtered or evaporated, we do not know if the results presented here are applicable to such materials. Since defect centers are apparently being formed and destroyed constantly while illuminated and in contact with either adsorbed or, equivalently, gas phase oxygen, we suggest the formation/destruction process also occurs isotropically.

At the defect densities studied, we found no evidence suggesting a large amount of cooperativity in the formation of CS structures. However, any degree of cooperativity would probably be a function of the laser power density involved. Since we are using sub band-gap irradiation to drive the photochemistry, the actual absorbing centers seem to be the defects themselves and the net absorption crosssection would not be expected to be very large. If some processes are only significant at high densities of "excited" defect centers, then the initial density of defects and the proportion of them which are excited at any instant in time will be expected to have a significant effect on what kind of photochemistry ensues. By "excited" defects we mean defect structures which have just participated in photon absorption. It is possible that we conducted our experiments at defect densities which are too low to allow observation of cooperative effects.

### 3.5.5 Conclusions

The distribution of Raman scattering centers, i.e. corner-sharing octahedra, on the surface of common  $WO_3$  is spatially uniform. The density of defects, i.e. edge-sharing, oxygen deficient octahedra, scales as the square of the lateral extent of the observed region as does the topographical surface area. At the power densities employed and the amount of oxygen substoichiometry employed, there appears to be little cooperativity between the chemistry occurring at different defect centers.

## 4. Conclusion

### 4.1 These Experiments

Oxides in general have plenty of defects. The wide range of power indices at different incident power ranges in these experiments show the complicated nature of oxides. In  $WO_3$ , there are plenty of defect states available to undergo transitions at 532 nm. This shows that there may be no lower power limit for the read beam, if the read beam is 532 nm. We may have to read at a different wavelength further away from the bandgap of  $WO_3$ , which is about 350 nm.

The exponential/logarithmic nature of our results when the 1.06  $\mu m$  power is ramped up (Figure 21) implies that the 1.06  $\mu m$  is acting mostly as heat, not as a transition source. Oxygen exchange with the atmosphere must be taken into account. As you heat up the medium, you desorb surface adsorbed gases, including oxygen. This changes the rate at which oxygen can leave the lattice itself, thus changing the rate at which octahedra reform to share edges. The fact that the Arrhenius plot of the 1.06  $\mu m$  ramp data (Figure 25) is not linear indicates that the optical process is not straightforward random heating. We know that the material is absorptive at near IR wavelengths. We also used high peak power modelocked and Q-switched pulse trains. The combination of these two factors may have led to a nonlinear transformation and absorption process.

In the 532 nm ramp data with constant 1.06  $\mu m$  present, there is no turnover peak at 90 mW and no further drop to the baseline, as there is in the 532 nm ramp alone data. The lack of turnover may be due to the IR keeping the lattice too warm to reconstruct into edge sharing octahedra. We should see if there is enough variation to work the system at the power density level for 532 nm light of  $650 \mu W/\mu m^2$ , and for 1.06  $\mu m$  light of  $520 \mu W/\mu m^2$ .

Although one of our Raman noise experiments showed a 19% standard deviation, this is still a much better read process, due to the zero signal on a written area, than any current optical recording system. It does, however, show that for the purpose of these and coming experiments, every dip and peak should be redone on a different area to make sure it is repeatable, and thus real.

The distribution of Raman scattering centers, i.e. corner-sharing octahedra, on the surface of common  $WO_3$  is spatially uniform. The density of defects, i.e. edge-sharing, oxygen deficient octahedra, scales as the square of the lateral extent of the observed region as does the topographical surface area. At the power densities employed and the amount of oxygen substoichiometry employed, there appears to be little cooperativity between the chemistry occurring at different defect centers.



## **4.2 Further Experiments**

The planned excitation spectra and direct sequence of transition measurements were not performed as the system was down for six months due to laser modelocker and Q-switch failure followed by OMA detector failure.

We should spatially displace the two wavelengths to help determine the thermal transfer properties of the photochromic material.

Our next step will be to use a tunable dye laser system to measure the excitation spectrum of the material. This will tell us where the Raman signal from the material is most enhanced by resonance.

Our final step will be to use a third color displaced temporally after the blue-green and IR together. The change in reflectance and/or transmission of the third color pulse as it is stepped away from the write pulses in time, will give us information about the timing and sequencing of the light absorption, electron transitions, lattice restructuring and intervalence transfer occurring in the material.

We were also disappointed in the power levels needed to write the material. We should do the same experiments in the UV. The bandgap of the material is at about 350 nm, so working in the UV should give us many more transition states, which should lead to lower power requirements for writing.

## **4.3 Payoff**

Successful completion of this proposed effort will lead to faster, more stable optical memory systems for Air Force mission planners, pilots needing mission maps and threat databases, intelligence data storage, and for other uses.

- <sup>1</sup>Duffy, J.A., *Bonding, Energy Levels and Bands in Inorganic Solids*, p. 185, Longman, 1990.
- <sup>2</sup>Salje, E., *Acta Cryst.*, **B33**, 574-577, (1977)
- <sup>3</sup>Cox, P.A., *Transition Metal Oxides*, p. 22, Clarendon Press, Oxford, 1992.
- <sup>4</sup>Eyring, L. and Tai, L., *The Structural Chemistry of Some Complex Oxides*, in Hannay, N.B., *Treatise on Solid State Chemistry Vol. 3*, Plenum, 1976.
- <sup>5</sup>Iguchi, E. and Tilley, R.J.D., *Journ. Solid State Chem.* **21**, 49-56 (1977).
- <sup>6</sup>Wells, A.F., *Structural Inorganic Chemistry*, p. 571, Clarendon Press, Oxford, 1984.
- <sup>7</sup>Tilley, R.J.D., *The Crystal Chemistry of the Higher Tungsten Oxides*, in Bartha, L. *et al.*, Eds., *The Chemistry of Non-Sag Tungsten*, p. 100, Pergamon, 1995.
- <sup>8</sup>Cox, P.A., *Transition Metal Oxides*, p. 48, Clarendon Press, Oxford, 1992.
- <sup>9</sup>Holl, M.M. and Penner-Hahn, J.E., *Chemistry 302 Lecture Summary*, University of Michigan Chemistry Department, on WWW as <http://www.umich.edu/~chem302/lecturesummary/wo3/index.html>, 1997.
- <sup>10</sup>Berak, J. & Sienko, M., *Journ. Solid State Chem.* **2**, 109-133 (1970).
- <sup>11</sup>Gandhi, S. & Bernstein, R.B., *Chem. Phys.* **105**, 423-430, (1986).
- <sup>12</sup>Winter, E.R.S., *J. Chem. Soc. (A)*, 2889-2902, (1968).

**Appendix A. A Surface Raman and Scanning Tunneling  
Microscopy Study of the Spatial Distribution of  
Corner-sharing and Edge-sharing Octahedra on Thermally  
Oxidized Tungsten**

Matthew Côté, Corey Radloff, Joseph M. Osman, Rebecca Bussjager, R. Martin Villarica,  
Fazio Nash, and J. Chaiken

To be published in "Chemical Aspects of Electronic Ceramics Processing", *Proceedings of  
the Material Research Society*, Vol. 495.

# A SURFACE RAMAN AND SCANNING TUNNELING MICROSCOPY STUDY OF THE SPATIAL DISTRIBUTION OF CORNER-SHARING AND EDGE-SHARING OCTAHEDRA ON THERMALLY OXIDIZED TUNGSTEN

Matthew J. Côté\*, Corey Radloff\*, Joseph M. Osman<sup>§</sup>, Rebecca Bussjager<sup>§</sup>, R. Martin Villarica<sup>†</sup>, Fazio Nash<sup>‡</sup>, J. Chaiken<sup>‡</sup>

\*Department of Chemistry, Bates College, Lewiston, Maine 04240

<sup>§</sup>Rome Laboratory, Rome, New York 13441-4515

<sup>†</sup>Laser Chemical Corporation, 302 Edwards Dr., Fayetteville, New York 13066, jchaiken@syr.edu

<sup>‡</sup>Department of Chemistry, Syracuse University, Syracuse, New York 13244-4100

## Abstract

We have measured the dependence of the strength of Raman activity of polycrystalline m-WO<sub>3</sub> on spot size at constant laser power density. These data are compared to surface area scaling measurements obtained using scanning tunneling microscopy. We argue that the spatial distribution of scattering centers is the complement of the spatial distribution of crystallographic shear (CS) structures on or near the oxide surface. Our results are consistent with there being an essentially uniform spatial distribution of scattering sites which implies the spatial distribution of defect sites is also uniform. At the laser power density involved and at the defect densities studied, we found no evidence suggesting a large amount of cooperativity in the formation of CS structures. These results suggest a qualitative description of the structure of common oxide surfaces in agreement with a basic assumption of the JMAK theory of first order phase transformations.

## Introduction

It has been known for some time<sup>1</sup> that absorption of a single photon with energy equal to or greater than the bandgap can drive the photochromic response of monoclinic tungsten oxide (m-WO<sub>3</sub>). We recently reported new results<sup>2,3</sup> demonstrating the use of sub band-gap laser excitation to manipulate the oxidation states, and the associated photochromic response, of the metal oxide. In our view<sup>3</sup>, sub band-gap excitation, involves surface or near-surface localized defect states and results in the formation of oxygen atoms. Mobility of oxygen atoms and oxygen vacancies leads to coalescence growth of structures known as crystallographic shear (CS) planes<sup>4</sup>. CS structures can be of varying sizes and orientations with respect to the gas-solid interface across which laser driven oxygen exchange occurs. ESCA spectra of oxygen deficient samples we have prepared, show only the presence of W<sup>+6</sup> and W<sup>+5</sup> species with the W<sup>+5</sup> species being associated with the blue, edge-sharing material.

The structure of m-WO<sub>3</sub> surfaces that exist in equilibrium with ambient air have been studied extensively<sup>5</sup>. The vibrational spectroscopy<sup>6</sup> of m-WO<sub>3</sub> has been studied by many groups and most features have been assigned unambiguously. There are two particularly strong and important features at 716 and 805 cm<sup>-1</sup> which are associated with the presence of corner sharing octahedra comprising the lattice of the idealized m-WO<sub>3</sub> structure. In the idealized structure it is thought that perfect m-WO<sub>3</sub> possesses a distorted ReO<sub>3</sub> type structure. The oxygen deficient material, m-WO<sub>3-x</sub>, accommodates the associated oxygen vacancies by a partial shift to edge sharing between the octahedra. The edge sharing octahedra do not give rise to any Raman features at or near 716 and 805 cm<sup>-1</sup> so that the strength of these features is a measure of the defect number density within the scattering volume. We have published<sup>3</sup> the O<sub>2</sub> pressure dependence of the Raman activity which strongly suggests that the edge and corner sharing octahedra are in a binary equilibrium.

We are interested in the earliest example of an exactly solvable, although phenomenological and stochastic, kinetic model of a first order phase transformation: the Kolmogorov<sup>7</sup>-Johnson-Mehl<sup>8</sup>-Avrami<sup>9</sup> (JMAK) theory. The JMAK model makes the assumption that macroscopic scale transformations begin at surface defect sites, presumably like those associated with surface defect sites in WO<sub>3</sub>. It is further assumed that the chemical transformation(s) associated with the phase

transition spread outward from each defect until regions of transformed phase originating from adjacent defects contact and terminate each other. This model allows the calculation of grain size distributions if the initial defect density and the rate at which the transformation spreads outward are known. This JMAK theory is often applied although there seems to be little experimental evidence refuting or supporting the idea.

Recently, there has been much work on the use of scanning probe microscopy<sup>10,11,12</sup>, in particular scanning tunneling microscopy (STM), to study CS structures on m-WO<sub>3</sub>. Allowing the possibility of atomic scale imaging, STM is a powerful tool for the study of conducting or semiconducting surfaces. STM data can give a direct measure of surface area on angstrom to micron spatial scales. In this study we compare the scaling of the surface area measured by STM to the size of the region scanned. Rough surfaces have greater surface area for a given projection along the x and y axes than would a perfectly flat surface with equal extent along the x and y axes.

To complement STM probing of the m-WO<sub>3</sub> surface, we have also used the Raman spectrum to assess the presence of corner sharing octahedra. We seek to test the validity of considering the entire surface to be composed of only corner-sharing, Raman active octahedra or edge-sharing, Raman inactive octahedra. If this picture is valid then the spatial distribution of defect centers and the spatial distribution of scattering centers are complementary. STM provides a measure of topographical area. If the total Raman intensity scales differently with increasing spot size than does the topographical area with the size of the scanned region, then the spatial distribution of scattering centers is not uniform within the scattering volume. Given the complexity of oxide surfaces, particularly those in contact with a crude ambient atmosphere, this comparison represents an unusual and possibly useful approach for characterizing the surfaces of metal oxides.

## Experimental

The Raman spectrometer has been described in detail elsewhere<sup>2</sup>. The excitation source was an Ar<sup>+</sup> ion laser operating on the 488 nm line. Spot size measurements were made using the moving knife edge-based technique implemented in the Spot Scan instrument (Photon, Inc.). For the present experiments, optics were added so that it was possible to view the laser irradiated region from which Raman shifted photons were collected. The small depth of focus employed in our experiments could be viewed directly on the active surface. This ensured that the focus size we measured using the Spot Scan was identical to the focus size that was employed in obtaining the Raman measurements of the WO<sub>3</sub> surface. Throughout our work, the spot shape was circular to visual examination and always easily fit using a Gaussian profile. The spot size for our purposes is defined arbitrarily as the 1/e point of the circularly symmetric spots.

The STM used for the surface area measurements comprises two horizontally oriented concentric piezo tubes both with outer electrodes separated into quadrants, as introduced by Binnig and Smith<sup>13</sup>. The inner piezo tube (6.4 mm diameter, 12.7 mm length) is used to scan the tip. The outer piezo tube (12.7 mm diameter, 12.7 mm length) is used to position the sample relative to the tip scanner. Identical cycloid shaped pulses applied to all quadrants of the outer piezo tube, relative to its grounded inner electrode, induce a "stick-slip"<sup>14</sup> motion of the sample holder toward or away from the STM tip, depending on the pulses' polarity. Applying pulses of opposite polarity to the left and right quadrants induces the stick-slip motion in the plane of the sample. Reproducible steps as small as 7 nm can be taken along either axis. Also, DC voltage offsets applied to the outer piezo tube quadrants can be used for fine positioning of the sample along x, y, and z. Tip height images were typically obtained using a scan speed of 4 lines per second.

The samples of m-WO<sub>3</sub> used for this study were obtained by thermal oxidation of tungsten foils. Tungsten metal foils of varying thickness (0.025 cm, 0.050 cm, 0.10 cm) were obtained from Aldrich Chemical and were used as received. The foil was cut into a roughly 1 cm x 1 cm square and put into a quartz boat which was placed into a tube furnace at 600 °C in ambient air. The foil became coated with a strongly adherent bright yellow oxide coat on the order of  $\approx 10^2$   $\mu$ m thick after  $\approx 20$ -25 minutes. Reflectance IR spectra of these oxidized foils are essentially identical to the spectra obtained from powder WO<sub>3</sub> also obtained from Aldrich Chemical. By direct comparison with powder samples, precession x-ray photographs of the oxidized foil also showed only the presence of W metal and WO<sub>3</sub>. The tungsten metal could only be detected by x-ray if the foil had not been oxidized thoroughly. Profilometry was performed using a Tencor Alpha-Step 500.

## Results

The Raman spectrum of the oxidized metal foils is identical to those published earlier<sup>3</sup> for  $\text{WO}_3$  powder ( $10\ \mu\text{m}$  particle size). Figure 1 shows the dependence of the peak Raman signal at the  $805\ \text{cm}^{-1}$  peak as a function of spot size for an essentially constant,  $1.91\ \text{mW}/\mu\text{m}^2$ , power density. To obtain these data, a spot was chosen on the oxidized surface of a foil and the Raman spectrum was obtained successively until there was no change, typically one or two seconds total exposure. The spectrum lost about 5-10% of the initial scattered intensity during this equilibration process. At this point, the oxide sample was equilibrated with the excitation at the ambient temperature and air pressure. By equilibrated, we mean that the net proportion of  $\text{WO}_3$  present compared with all non-Raman scattering  $\text{WO}_x$  type species was considered constant while the light was on.

Having established an equilibrated spot on the oxide, the spot size was measured and power density was calculated. By changing the distance between the focusing objective and the sample surface, the spot size was varied. The spot size was re-measured each time the sample to objective distance was changed to ensure accuracy. Using the calculated power density from the previous measurement, the power of the laser was varied so as to keep the power density constant. In this way, successive Raman spectra were obtained in which the laser power density impinging on the sample surface was constant while the spot size was varied.

To avoid systematic error, the spot size was varied such that no two successive measurements were made which varied in the same magnitude or sign. However, the spot size was always varied by moving the focusing objective closer to the sample surface than the position which obtains the smallest spot. The uncertainty, 1 standard deviation, in the least squares slope for each of these plots, without including any uncertainty in the raw Raman counts, was such that each slope was 2.0. Thus, Figure 1 clearly shows that the variation in Raman signal, corresponding to a factor of three variation in spot size, is accounted for in terms of a quadratic variation.

Samples of oxidized foil were imaged using the STM at various degrees of spatial resolution and scan size. Representative images are displayed in Figure 2. Similar scan parameters modes were employed for all images. Profilometry showed that over any randomly chosen region on the surface in the range of  $10\ \mu\text{m}$  to  $1\ \text{mm}$ , there are vertical excursions in the range given by

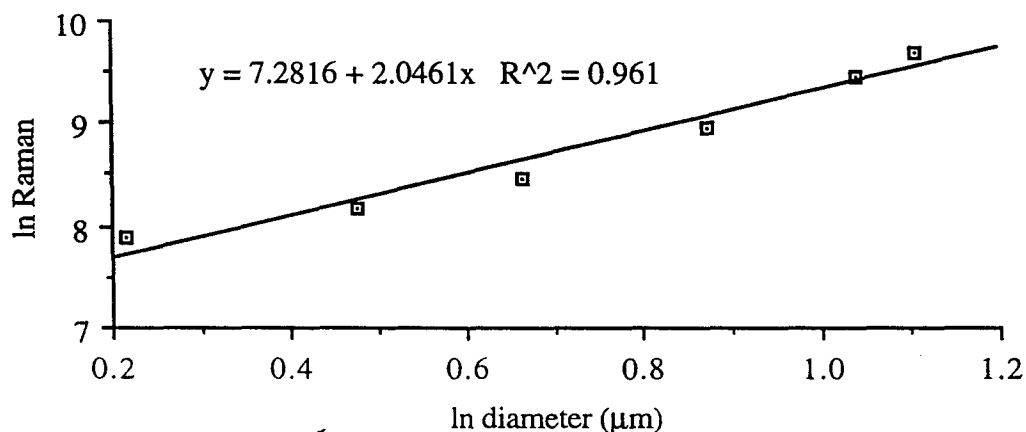


Figure 1. Dependence of Raman counts on spot size at constant laser power density

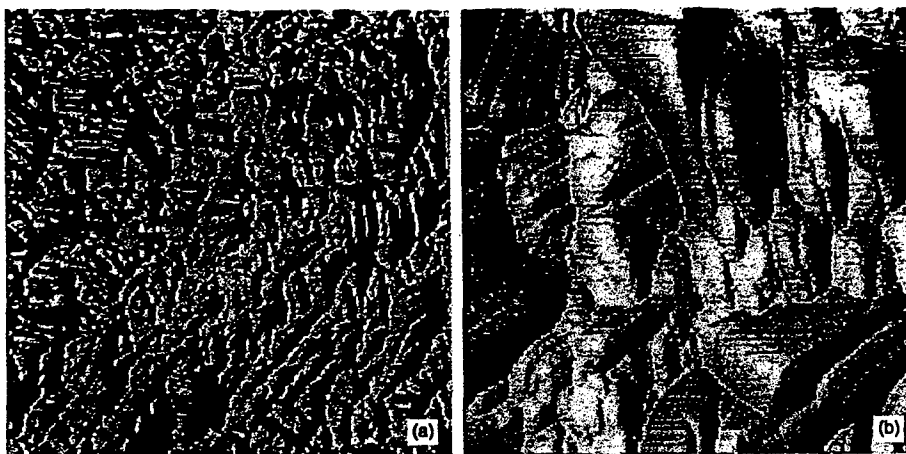


Figure 2 Typical STM images of a thermally oxidized tungsten foil sample. (0.5 V tip bias and current set point of 0.5 nA) (a) 1.8  $\mu\text{m}$  square, (b) 380 nm square

the RMS corrugation. The STM images reveal a rich diversity of topographies on all scales, however, for our present purposes, we are concerned only with how the oxide surface area scales with the lateral extent of the region imaged.

To obtain the topographical surface area from a particular STM image we recognize that the raw data is a collection of  $(x, y, z)$  points which comprise the location of the surface detected by the scanning probe. Each surface area calculation was based on an STM image that consisted of 65536 height( $z$ ) measurements taken on a square  $256 \times 256$  ( $x, y$ ) grid. The STM images take the form of height measurements which we stored as a  $256 \times 256$  array,  $I$ . From  $I$ , a  $255 \times 255$  element surface array  $A$  was computed as follows:

$$A_{m,n} = \frac{1}{2} \Delta x \sqrt{(I_{i,j+1} - I_{i,j})^2 + (I_{i+1,j} - I_{i,j})^2 + \Delta x^2} + \sqrt{(I_{i,j+1} - I_{i+1,j+1})^2 + (I_{i+1,j} - I_{i+1,j+1})^2 + \Delta x^2} \quad (1)$$

where  $\Delta x$  is the horizontal distance between neighboring measurement sites, and  $\{I_{i,j}\}$  are height measurements. Surface area array element  $A_{0,0}$ , for example, was obtained by summing the surface areas of the two triangular regions corresponding to  $I_{0,1}$ ,  $I_{0,0}$ ,  $I_{1,0}$  and  $I_{0,1}$ ,  $I_{1,1}$ ,  $I_{1,0}$ , taking into account each region's angle of inclination. The total surface area of the scanned area is the sum of the elements in  $A$ .

To study a sample's surface area as a function of projected area, a log-log plot of the surface area lying within a circle of radius  $r$ , was created as a function of  $r$ . The slope of the resulting line is the surface fractal dimension. Mild smoothing of images was used to reduce high frequency noise before surface areas were computed. Neither the computed surface areas nor the computed surface fractal dimension was found to depend significantly upon the extent or type (convolution or median) of filtering employed.

Using this algorithm, we measured the surface area as a function of projected area for several regions of several samples. The variation of the calculated surface area with the size of the  $x, y$  range for four such images can be seen in Figure 3. Despite the wide variation in appearance, every region examined showed that the surface area scales as the square of the lateral extent of the image. In the language of the fractal literature, the surface fractal dimension of oxide surfaces prepared using our procedure is 2.

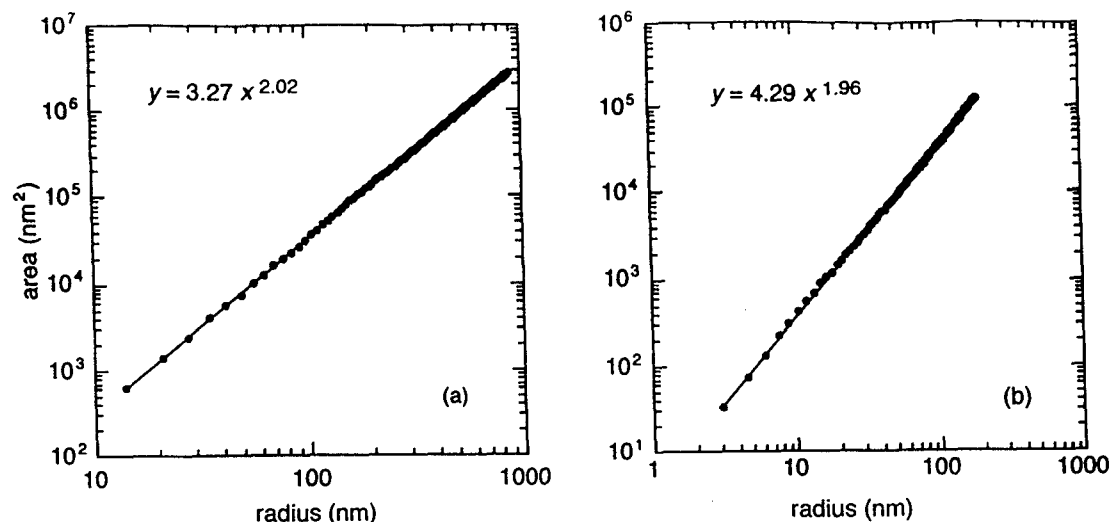


Figure 3 Surface area calculated from topographic data (see text) (a) and (b) are calculated from images 2a and 2b respectively

### Discussion

We performed these Raman experiments at constant power density for two reasons. First, we wanted to have a constant penetration depth of the light into the oxide surface so that whatever variation in Raman strength was observed could be interpreted in terms of the increasing lateral extent of the exposed region. Second, from our earlier work, we knew that the degree of oxygen substoichiometry, as will be discussed below, would be a function of the applied power density. If the power density was not constant then the degree of substoichiometry would have varied.

The Raman scattering and STM imaging results show that both the density of Raman scatterers and the topographical area vary as the square of the lateral extent of the region examined. The STM images define the surface of constant tunneling current indicated by the  $z$  coordinates. This would be expected if the Raman scattering centers were uniformly distributed across the oxide surface. Since we presume that the regions of edge sharing octahedra and corner sharing octahedra are complementary, this finding also suggests that the density of defects varies as if their spatial distribution were isotropic across the oxide surface.

The Raman experiments probed a region which is very large compared to the largest expected dimension of the CS planes so that we do not expect to be able to discern any structural features of individual CS planes. We assume that a large number always tended to be completely enveloped by the observation process. Since the Raman intensity varies quadratically with the spot size, we conclude that the spatial distribution of CS structures is uniform.

It should be noted that we have attempted to characterize the most common type of tungsten oxide one can prepare. Because of the inherent anisotropy or extremely small grain size of columnar sputtered films or highly amorphous evaporated films respectively, we do not know if the results presented here are applicable to such materials. Since defect centers are apparently being formed and destroyed constantly while illuminated and in contact with either adsorbed or, equivalently, gas phase oxygen, we suggest the formation/destruction process also occurs isotropically.

At the defect densities studied, we found no evidence suggesting a large amount of cooperativity in the formation of CS structures. However, any degree of cooperativity would probably be a function of the laser power density involved. Since we are using sub band-gap irradiation to drive the photochemistry, the actual absorbing centers seem to be the defects themselves and the net absorption crosssection would not be expected to be very large. If some processes are only significant at high densities of "excited" defect centers, then the initial density of defects and the proportion of them which are excited at any instant in time will be expected to have a significant effect on what kind of photochemistry ensues. By "excited" defects we mean defect structures which have just participated in photon absorption. It is possible that we conducted our experiments at defect densities which are too low to allow observation of cooperative effects.



## Conclusions

The distribution of Raman scattering centers, i.e. corner-sharing octahedra, on the surface of common  $\text{WO}_3$  is spatially uniform. The density of defects, i.e. edge-sharing, oxygen deficient octahedra, scales as the square of the lateral extent of the observed region as does the topographical surface area. This finding supports the basic assumption of the JMAK theory of first order phase transitions in metal oxide systems. At the power densities employed and the amount of oxygen substoichiometry employed, there appears to be little cooperativity between the chemistry occurring at different defect centers.

## Acknowledgments

This research was supported by Rome Laboratory, the Research Corporation, a grant to Bates College from the Howard Hughes Medical Institute, and Laser Chemical Corporation. The authors gratefully acknowledge Professor John Rhodes (Bates College) for assistance with the surface area algorithm. Conversations with Professor Jerry Goodisman were also helpful.

## References

1. S. K. Deb, Appl. Opt. 801(1972), Philos. Mag. 27, 801(1973)
2. Joseph M. Osman, Rebecca J. Bussjager, Fazio Nash, R. M. Villarica, J. Chaiken, Appl. Phys. A. in press
3. R. M. Villarica, Fazio Nash, Joseph M. Osman, Rebecca J. Bussjager, J. Chaiken, Proc. Mat. Res. Soc. 397, 347(1996)
4. M. Sundberg, R. J. D. Tilley, J. Solid State Chem. 11, 150-160(1974)
5. C. G. Granquist, "Handbook of Inorganic Electrochromic Materials"(Elsevier, Amsterdam, 1995)
6. M. F. Daniel, B. Desbat and J. C. Lassegues, J. Solid State Chem. 73, 127-139(1988), J. Solid State Chem. 67, 235-247(1987)
7. A. N. Kolmogorov, Izv. Akad. Nauk SSSR, Ser. Matem No. 3, 355-359(1937)
8. W. Johnson and R. F. Mehl, TAIME 135, 416-442, Discussion 442-458(1939); unpublished details of the derivations in Appendices A-E deposited as ADI number 1182 with the American Society for Information Science (ISIS), 8720 Georgia Avenue, Silver Spring, MD 20910-3603.
9. Melvin Avrami, J. Chem. Phys. 7, 1103-1112(1939), J. Chem. Phys. 8, 212-224(1940), J. Chem. Phys. 9, 177-184(1941)
10. F. H. Jones, K. Rawlings, J. S. Foord, R. G. Egdell, J. B. Pethica, B. M. R. Wanklyn, S. C. Parker, P. M. Oliver, Surf. Sci. 359, 107-121(1996)
11. F. H. Jones, K. Rawlings, J. S. Foord, P. A. Cox, R. G. Egdell, J. B. Pethica, B. M. R. Wanklyn, Phys. Rev. B. 52, R14 392-R14 395(1995-II)
12. F. H. Jones, R. A. Dixon, A. Brown, Surf. Sci. 369, 343-350(1996)
13. G. Binnig and D. P. E. Smith, Rev. Sci. Instrum. 57, 1688(1986).
14. "stick-slip", or "inertial drive", translator first described by D. W. Pohl, Rev. Sci. Instrum. 58, 54(1987).

**Appendix B. A Surface Raman-Scanning Tunneling  
Microscopy Study of the Spatial Distribution of  
Corner-sharing and Edge-sharing Octahedra on Thermally  
Oxidized Tungsten**

Matthew Côté, Corey Radloff, Joseph M. Osman, Rebecca Bussjager, R. Martin Villarica,  
Fazio Nash, and J. Chaiken

Submitted to *Phys. Rev A*.

**A SURFACE RAMAN-SCANNING TUNNELING MICROSCOPY STUDY OF THE  
SPATIAL DISTRIBUTION OF CORNER-SHARING AND EDGE-SHARING  
OCTAHEDRA ON THERMALLY OXIDIZED TUNGSTEN**

Matthew J. Côté, Corey Radloff, Department of Chemistry, Bates College, Lewiston, Maine 04240; Joseph M. Osman, Rebecca Bussjager, Rome Laboratory, Rome, New York 13441-4515; R. Martin Villarica, Laser Chemical Corporation, 302 Edwards Dr., Fayetteville, New York 13066-1008; Fazio Nash, J. Chaiken, Department of Chemistry, Syracuse University, Syracuse, New York 13244-4100

**Abstract**

We have measured the dependence of the strength of Raman activity of polycrystalline  $m\text{-WO}_3$  on spot size at constant laser power density. These data are compared to surface area scaling measurements obtained using scanning tunneling microscopy to deduce characteristics of the spatial distribution of scattering centers on the oxide surface. Because observations are consistent with the idea that edge sharing and corner sharing octahedra are involved in a binary equilibrium, we argue that the spatial distribution of scattering centers is the complement of the spatial distribution of defect centers and crystallographic shear structures on or near the oxide surface. Our results are consistent with there being an essentially uniform spatial distribution of scattering sites. We therefore deduce that the spatial distribution of defect sites is also uniform. These results suggest a qualitative description of the structure of common oxide surfaces which justifies a basic assumption the JMAK theory of first order phase transformations, and may be useful for applications such as barrier layers, photocatalysis and optical memory.

## Introduction

It has been known for some time<sup>1</sup> that absorption of a single photon with energy equal to or greater than the bandgap can drive the photochromic response of monoclinic tungsten oxide ( $m\text{-WO}_3$ ). We recently reported new results<sup>2,3</sup> demonstrating the use of sub band-gap laser excitation to manipulate the oxidation states of transition metal oxides and the associated photochromic response. The particular case of powdered room temperature  $m\text{-WO}_3$  was used to show how the metal-oxygen stoichiometry, i.e. phase equilibrium, depended on the applied laser power, the temperature, and the oxygen partial pressure. Later, we showed that infrared irradiation could be substituted for bulk heating of the medium suggesting an all optical erasable digital memory process. Having identified the basic parameters governing the observed laser-mediated oxygen exchange chemistry, we plan to investigate each in greater detail in the present and future studies.

On the basis of the expected atomic orbital parentage in  $\text{WO}_3$ , super band-gap excitation accesses delocalized states having antibonding character with respect to the W-O bonds. In our view<sup>3</sup>, sub band-gap excitation is effective in promoting transitions between different metal-oxide phases because the initial excitation event involves surface or near-surface localized defect states. Since sub band-gap excitation is effective in promoting oxygen exchange, we surmise both that the absorbing entities are associated with defects and/or surfaces that intrinsically occur in  $m\text{-WO}_3$  and also that upon excitation they somehow induce W-O bond weakening.

The structure of  $m\text{-WO}_3$  has been studied extensively<sup>4</sup>. We are interested in surfaces that exist in equilibrium with ambient air and this allows many possibilities. The vibrational spectroscopy<sup>5</sup> of  $m\text{-WO}_3$  has been studied by many groups and most features have been assigned unambiguously. There are two particularly strong and important features at 716 and 805  $\text{cm}^{-1}$  which are associated with the presence of corner sharing octahedra comprising the lattice of the idealized  $m\text{-WO}_3$  structure. In the idealized structure it is thought that perfect  $m\text{-WO}_3$  possesses a distorted  $\text{ReO}_3$  type structure. The oxygen deficient material,  $m\text{-WO}_{3-x}$ , accommodates the associated oxygen vacancies by a partial shift to edge sharing between the octahedra. The edge sharing octahedra do not give rise to any Raman features at or near 716 and 805  $\text{cm}^{-1}$  so that the strength of these features is a measure of the defect number density within the scattering volume. We have published<sup>3</sup> the  $\text{O}_2$  pressure dependence of the Raman activity which strongly suggests that the edge and corner sharing octahedra are in a binary equilibrium. If there is any other type of surface present on  $m\text{-WO}_3$ , then it represents a constant fraction of the total physical surface, throughout the manipulation of the aforementioned binary equilibrium.

The edge sharing octahedra are mobile, presumably by the simple shifting of bonds, oxygen atoms, and oxygen vacancies and not by the wholesale motion of tungsten atoms. This mobility leads to the formation by coalescence growth of structures known as crystallographic shear (CS) planes<sup>6</sup>. CS structures can be of varying sizes and orientations with respect to the gas-solid interface. ESCA spectra of oxygen deficient samples we have prepared using purely optical

methods, which means no conductive or convective heating, show only the presence of  $W^{+6}$  and  $W^{+5}$  species with the  $W^{+5}$  species being associated with the blue, edge-sharing material. Experiments<sup>6</sup> using thoroughly degassed and dehydrated samples suggest that the chemistry which we use to form  $W^{+5}$ -rich materials from ostensibly pure  $W^{+6}$  material occurs in the absence of water, hydrogen or any other proton donor.

Many important chemical, electrical and optical processes occur with enhanced efficiency at the defect sites of metal oxides. In order to better understand surfaces, and perhaps construct improved models, we are interested in probing the spatial distribution of defect sites. Given sufficient details concerning the relevant probability distribution functions of the defects, having the ability to accurately model processes at individual sites could allow one to build up a description of a macroscopic surface. As an example of how this can be done, consider the earliest example of an exactly solvable, although phenomenological and stochastic, kinetic model of a first order phase transformation: the Kolmogorov<sup>7</sup>-Johnson-Mehl<sup>8</sup>-Avrami<sup>9</sup> (JMAK) theory.

The JMAK model makes the assumption that macroscopic scale transformations begin at surface defect sites, presumably like those associated with surface defect sites in  $WO_3$ . It is further assumed that the chemical transformation(s) associated with the phase transition spread outward from each defect until regions of transformed phase originating from adjacent defects contact and terminate each other. This model allows the calculation of grain size distributions if the initial defect density and the rate at which the transformation spreads outward are known. This JMAK theory is often applied even if the basic assumptions are not rigorously met because it often gives qualitatively correct predictions. In particular, the JMAK theory is based on the assumption that the initial spatial distribution of defects is uniform and random, although there seems to be little experimental evidence refuting or supporting the idea.

We believe there is a correlation between the net defect density, the level of oxygen deficiency, and the presence of edge-sharing octahedra and larger scale structural features like CS planes. Recently, there has been much work on the use of scanning probe microscopy<sup>10,11,12</sup>, in particular scanning tunneling microscopy (STM), to study CS structures on  $m-WO_3$ . Allowing the possibility of atomic scale imaging, STM is a powerful tool for the study of conducting or semiconducting surfaces. STM data can give a direct measure of surface area on angstrom to micron spatial scales. In this study we compare the scaling of the surface area measured by STM to the size of the region scanned. Rough surfaces have greater surface area for a given projection along the x and y axes than would a perfectly flat surface with equal extent along the x and y axes.

To complement direct probing of the  $m-WO_3$  surface, we have also used the Raman spectrum to assess the presence of corner sharing octahedra. We seek to test the validity of considering the entire surface to be composed of either corner-sharing, Raman active octahedra or edge-sharing, Raman inactive octahedra. If this picture is valid then the spatial distribution of defect centers and the spatial distribution of scattering centers are complementary. STM naturally provides a measure of topographical area. If the total Raman intensity scales differently

with increasing spot size than does the topographical area with the size of the scanned region, then the spatial distribution of scattering centers is not uniform within the scattering volume. Given the complexity of oxide surfaces, particularly those in contact with a crude ambient atmosphere, this comparison explores an unusual and possibly useful approach for characterizing the surfaces of metal oxides.

## Experimental

The Raman spectrometer has been described in detail elsewhere<sup>2</sup>. The excitation source was an Ar<sup>+</sup> ion laser operating on the 488 nm line. Laser power was measured and actively held constant with a 3-5 kHz servo bandwidth using a Cambridge Research Institute Laser Power Controller (model LPC-vis). Spot size measurements were made using the moving knife edge-based technique implemented in the Spot Scan instrument by Photon Inc. or using the imaging technique based Spiricon LB-100. Throughout our work, the spot shape was circular to visual examination and always easily fit using a Gaussian profile. The spot size for our purposes is defined arbitrarily as the  $1/e^2$  point of the circularly symmetric spots.

The diameters given in our results are those given by the knife edge method. We chose to use those values because of the dependence of the measurements obtained from the imaging technique on the thresholding of the detector. To obtain consistent measurements it is important that the detector not be saturated in the center of the distribution. As a practical matter the dynamic range of the detector limits the ability to establish and maintain an unbiased approach to calculating spot sizes. Thus, because it was easier to obtain consistent and unbiased thresholding, we considered the knife edge technique superior. For the present experiments, optics were added so that it was possible to view the exposed area under the same magnification as was being used to image the Raman excitation. The small depth of focus employed in our experiments could be viewed directly on the active surface. This ensured that the focus size we measured was identical to the focus size that was employed in obtaining the Raman measurements of the WO<sub>3</sub> surface.

The STM used for the surface area measurements comprises two horizontally oriented concentric piezo tubes<sup>13,14</sup> both with outer electrodes separated into quadrants, as introduced by Binnig and Smith<sup>15</sup>. The inner piezo tube (6.4 mm diameter, 12.7 mm length) is used to scan the tip. The outer piezo tube (12.7 mm diameter, 12.7 mm length) is used to position the sample relative to the tip scanner. Identical cycloid shaped pulses applied to all quadrants of the outer piezo tube, relative to its grounded inner electrode, induce a "stick-slip"<sup>16</sup> motion of the sample holder toward or away from the STM tip, depending on the pulses' polarity. Applying pulses of opposite polarity to the left and right quadrants induces the stick-slip motion in the plane of the sample. Reproducible steps as small as 7 nm can be taken along either axis. Also, DC voltage offsets applied to the outer piezo tube quadrants can be used for fine positioning of the sample along x, y, and z.

The control electronics are based on an analog feedback loop comprising an integrator and log circuit. A Macintosh Quadra 950 with National Instruments<sup>17</sup> A/D and D/A boards is used to

control the instrument and acquire and display data. Instrument control software was written using LabVIEW augmented by LabDQ<sup>18</sup> to speed data display. Tip height images were typically obtained using a scan speed of 4 lines per second.

The samples of m-WO<sub>3</sub> used for this study were obtained by thermal oxidation of tungsten foils. Tungsten metal foils of varying thickness (0.025 cm, 0.050 cm, 0.10 cm) were obtained from Aldrich Chemical and were used as received. The foil was cut into a roughly 1 cm x 1 cm square and put into a quartz boat which was placed into a tube furnace at 600 °C in ambient air. The foil became coated with a strongly adherent bright yellow oxide coat on the order of ~ 10<sup>2</sup> μm thick after ~20-25 minutes. Reflectance IR spectra of these oxidized foils are essentially identical to the spectra obtained from powder WO<sub>3</sub> also obtained from Aldrich Chemical. By direct comparison with powder samples, precession x-ray photographs of the oxidized foil also showed only the presence of W metal and WO<sub>3</sub>. The tungsten metal could only be detected by x-ray if the foil had not been oxidized thoroughly. Profilimetry was performed using a Tencor Alpha-Step 500.

## Results

A representative Raman spectrum of the oxidized metal foils is identical to those published earlier<sup>3</sup> for WO<sub>3</sub> powder (10 μm particle size). Figure 1 shows the dependence of the peak Raman signal at the 805 cm<sup>-1</sup> peak as a function of spot size. To obtain these data, a spot was chosen on the oxidized surface of a foil and the Raman spectrum<sup>3</sup> was obtained successively until there was no change, typically one or two seconds total exposure. The spectrum lost about 5-10% of the initial scattered intensity during this equilibration process. At this point, the oxide sample was equilibrated with the excitation at the ambient temperature and air pressure. By equilibrated, we mean that the net proportion of WO<sub>3</sub> present compared with all non-Raman scattering WO<sub>x</sub> type species was considered constant while the light was on.

Having established an equilibrated spot on the oxide, the spot size was measured and power density was calculated. By changing the distance between the focusing objective and the sample surface, the spot size was varied. The spot size was re-measured each time the sample to objective distance was changed to ensure accuracy. Using the calculated power density from the previous measurement, the power of the laser was varied so as to keep the power density constant. In this way, successive Raman spectra were obtained in which the laser power density impinging on the sample surface was constant while the spot size was varied.

It was not possible to exactly compensate for the spot size variation by varying the laser power so two plots can be seen in Figure 1. The upper plot corresponds to the raw data for which the power density was constant to within ±7% (one standard deviation). To normalize for this small variation, each raw data point (Raman counts) was divided by the measured power density which itself was divided by the average power (1.91 mW/μm<sup>2</sup>) density of the set. These points were plotted in the lower plot. Since the correction factor in each case was nearly unity, the normalized Raman counts only changed slightly.

To avoid systematic error, the spot size was varied such that no two successive measurements were made which varied in the same magnitude or sign. However, the spot size was always varied by moving the focusing objective closer to the sample surface than the position which brings the spot into focus. The uncertainty, 1 standard deviation, in the least squares slope for each of these plots, without including any uncertainty in the raw Raman counts, was such that each slope was 2.0. Thus, Figure 1 clearly shows that the variation in Raman signal, corresponding to a factor of three variation in spot size, is accounted for in terms of a quadratic variation.

Samples of oxidized foil were imaged using the STM at various degrees of spatial resolution and scan size. Representative images are displayed in Figure 2. Similar scan parameters modes were employed for all images. Profilimetry showed that over any randomly chosen region on the surface in the range of 10  $\mu\text{m}$  to 1 mm, there are vertical excursions in the range given by the RMS corrugation. The STM images reveal a rich diversity of topographies on all scales, however, for our present purposes, we are concerned only with how the oxide surface area scales with the lateral extent of the region imaged.

To obtain the topographical surface area from a particular STM image we recognize that the raw data is a collection of (x, y, z) points which comprise the location of the surface detected by the scanning probe. Each surface area calculation was based on an STM image that consisted of 65536 height(z) measurements taken on a square 256 x 256 (x,y) grid. The images take the form of height measurements which we stored as a 256 x 256 array, **I**. From **I**, a 255 x 255 element surface array **A** was computed as follows:

$$A_{m,n} = \frac{1}{2} \Delta x \sqrt{(I_{i,j+1} - I_{i,j})^2 + (I_{i+1,j} - I_{i,j})^2 + \Delta x^2} + \sqrt{(I_{i,j+1} + I_{i+1,j+1})^2 + (I_{i+1,j} - I_{i+1,j+1})^2 + \Delta x^2}$$

where  $\Delta x$  is the horizontal distance between neighboring measurement sites, and  $\{I_{i,j}\}$  are height measurements. Surface area array element  $A_{0,0}$ , for example, was obtained by summing the surface areas of the two triangular regions corresponding to  $I_{0,1}$ ,  $I_{0,0}$ ,  $I_{1,0}$  and  $I_{0,1}$ ,  $I_{1,1}$ ,  $I_{1,0}$ , taking into account each region's angle of inclination. The total surface area of the scanned area is the sum of the elements in **A**.

To study a sample's surface area as a function of projected area, a log-log plot of the surface area lying within a circle of radius  $r$ , was created as a function of  $r$ . The slope of the resulting line is the surface fractal dimension. Mild smoothing of images was used to reduce high frequency noise before surface areas were computed. Neither the computed surface areas nor the computed surface fractal dimension was found to depend significantly upon the extent or type (convolution or median) of filtering employed

Using this algorithm, we measured the surface area as a function of projected area for several regions of several samples. The variation of the calculated surface area with the size of the x,y range for four such images can be seen in Figure 3. Despite the wide variation in appearance, every region examined showed that the surface area scales as the square of the lateral extent of



the image. In the language of the fractal literature, the surface fractal dimension of oxide surfaces prepared using our procedure is 2.

## Discussion

We performed these Raman experiments at constant power density for two reasons. First, we wanted to have a constant penetration depth of the light into the oxide surface so that whatever variation in Raman strength was observed could be interpreted in terms of the increasing lateral extent of the exposed region. Second, from our earlier work, we knew that the degree of oxygen substoichiometry, as will be discussed below, would be a function of the applied power density. If the power density was not constant then the degree of substoichiometry would have varied.

The Raman scattering and STM imaging results show that both the density of Raman scatterers and the topographical area vary as the square of the lateral extent of the region examined. The STM images define the surface of constant tunneling current indicated by the  $z$  coordinates. This would be expected if the Raman scattering centers were uniformly distributed across the oxide surface. Since we presume that the regions of edge sharing octahedra and corner sharing octahedra are complementary, this finding also suggests that the density of defects varies as if their spatial distribution were isotropic across the oxide surface. We now consider whether it is possible to obtain the same quantitative observation without the distribution of defects being spatially isotropic.

We have shown previously<sup>3</sup> that under laser irradiation, such as was used to obtain the Raman spectra, the yellow  $\text{WO}_3$  material equilibrates with the local atmosphere. The equilibration process changes the relative proportions of edge and corner sharing octahedra comprising the oxide surface. These proportions are determined by the relative rates of photoinduced oxygen loss and oxygen reincorporation. Photoinduced oxygen loss results in formation of edge sharing octahedra and reincorporation results in formation of structures involving corner sharing octahedra. We suggest that defects are constantly being formed and destroyed during irradiation.

Many have suggested that the defects in question undergo coalescence growth to form CS planes. Edgell and coworkers<sup>10,11</sup> have recently published STM images obtained under UHV conditions of CS planes which complement TEM images which have been in the literature for some time. Under the conditions of our experiments we must ask whether the average size of CS planes remains very small relative to both the size of the smallest spot used to obtain the Raman data and the size of the regions explored with the STM. Based on Edgell's results, the CS planes themselves would seem to have a definite anisotropy which leaves open the possibility of observing scaling exponents other than 2. However, the anisotropy of a single CS plane would not be detectable unless the size of the region probed was about the same size.

In the case of the STM measurements, the regions probed span the entire range of possible sizes of the CS planes. However, the difference between STM images of CS planes and the surrounding regions is subtle. CS planes have different I-V characteristics than more oxygen-rich regions and the presence of adsorbed oxygen, such as was always present in our experiments but

was carefully manipulated in Edgell's measurements, would certainly obscure such subtle differences. Thus we expect the STM measurements to provide a good measure of topographical surface area in our experiments.

On the other hand, the Raman experiments probed a region which is very large compared to the largest expected dimension of the CS planes so that we do not expect to be able to discern any structural features of individual CS planes. We assume that a large number always tended to be completely enveloped by the observation process. X-ray crystallographic data, transmission electron microscopy (TEM) and recent STM work by Edgell and coworkers<sup>10,11</sup> on single crystal  $\text{WO}_3$  samples in UHV all suggest that the width of individual planes tends to be at least 15-20 Å. They also suggest that the planes terminate at the solid-gas interface at an elevation ( $z$  coordinate) which differs from the surrounding regions by at most  $\sim 1-2$  Å. Because the CS planes are composed of slightly distorted octahedra, 15-20 Å can also be taken as a gross indication of the size of a single "edge-sharing" octahedron.

Since the smallest region studied by Raman was  $\sim 6000$  Å across, this suggests that the longest planes could not involve the coalescence of much more than  $\sim 400$  individual edge sharing octahedra. Here we implicitly assume that the CS planes tend to be longer than they are wide as has been reported for some time in the literature<sup>9</sup> based on direct observation. In the present experiments, the Raman intensity lost due to photoinduced oxygen loss, and concomitant defect formation, is only on the order of 5 to 10%. Therefore it seems highly unlikely that we form a few single large structures having dimensions approaching the spot size. We therefore suggest that the variation in Raman intensity we observe with varying spot size is due to including or excluding CS structures which are always much smaller than the spot size from the irradiated spot. This is different from the case of overlapping more or less of a single large CS structure as the spot size is varied. Since the Raman intensity varies quadratically with the spot size, we conclude that the spatial distribution of CS structures is uniform.

To amplify on this conclusion we note that there may be a limit to the size of the CS planes which are formed under our conditions. Tilley and coworker<sup>19</sup> have suggested that, in the absence of strain and other external forces, there is an electrostatic repulsion between CS planes due to the increased electron density associated with the  $\text{W}^{+5}$  centers. However, it is also true that none of our measurements, or to our knowledge none of those reported in the literature, offer unequivocal information bearing directly on the extent of CS plane propagation below the oxide surface. TEM and STM measurements in the literature have involved sectioning, ion beam milling and annealing and in some cases polishing. We do not know if these forms of sample preparation could have a determining effect on the types of CS structures which can be formed and/or observed.

It should be noted that we have attempted to characterize the most common type of tungsten oxide one can prepare. Because of the inherent anisotropy or extremely small grain size of columnar sputtered films or highly amorphous evaporated films respectively, we do not know if the results presented here are applicable to such materials. Since defect centers are apparently being formed and destroyed constantly while illuminated and in contact with either adsorbed or,

equivalently, gas phase oxygen, we suggest the formation/destruction process also occurs isotropically.

Finally, at the defect densities studied, there is no evidence that there is a large amount of cooperativity in the formation of CS structures. However, any degree of cooperativity would probably be a function of the laser power density involved. Since we are using sub-band gap irradiation to drive the photochemistry, the actual absorbing centers seem to be the defects themselves and the net absorption crosssection would not be expected to be very large. If some processes are only significant at high densities of "excited" defect centers, then the initial density of defects and the proportion of them which are excited at any instant in time will be expected to have a significant effect on what kind of photochemistry ensues. By "excited" defects we mean defect structures which have just participated in photon absorption. It is possible that we conducted our experiments at defect densities which are too low to allow observation of cooperative effects.

## Conclusions

The distribution of Raman scattering centers, i.e. corner-sharing octahedra, on the surface of common  $\text{WO}_3$  is spatially uniform. The density of defects, i.e. edge-sharing, oxygen deficient octahedra, scales as the square of the lateral extent of the observed region as does the topographical surface area. This finding supports the basic assumption of the JMAK theory of first order phase transitions in metal oxide systems. At the power densities employed and the amount of oxygen substoichiometry employed, there appears to be little cooperativity between the chemistry occurring at different defect centers.

## Acknowledgments

This research was supported by Rome Laboratory, the Research Corporation, a grant to Bates College from the Howard Hughes Medical Institute, and Laser Chemical Corporation. The authors gratefully acknowledge Professor John Rhodes (Bates College) for assistance with the surface area algorithm. We have found a review article titled "The Time Cone Method for Nucleation and Growth Kinetics on a Finite Domain" by John W. Cahn (NIST) to be useful but we have not been able to find a adequate literature reference so we acknowledge the assistance here.

## Figure Captions

Figure 1 Dependence of Raman signal at  $805\text{ cm}^{-1}$  as a function of spot size at constant power density. The upper plot is the raw data and a least squares fit. The lower plot is the same data corrected for the slight variation in power density ( $\pm 5\%$ , see text) which was unavoidable as the spot size was changed. The uncertainty in the least squares slopes calculated without introducing any uncertainty in the raw data points for the corrected and uncorrected data are both approximately 0.2.

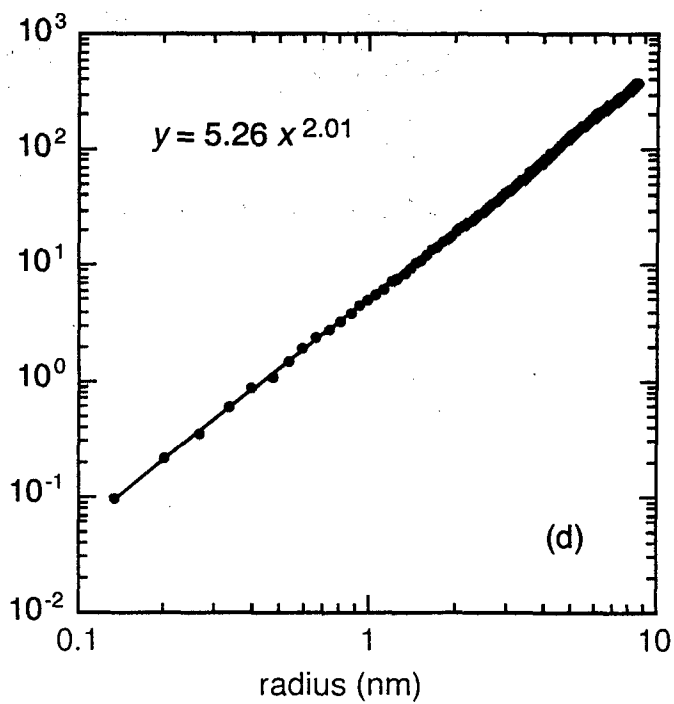
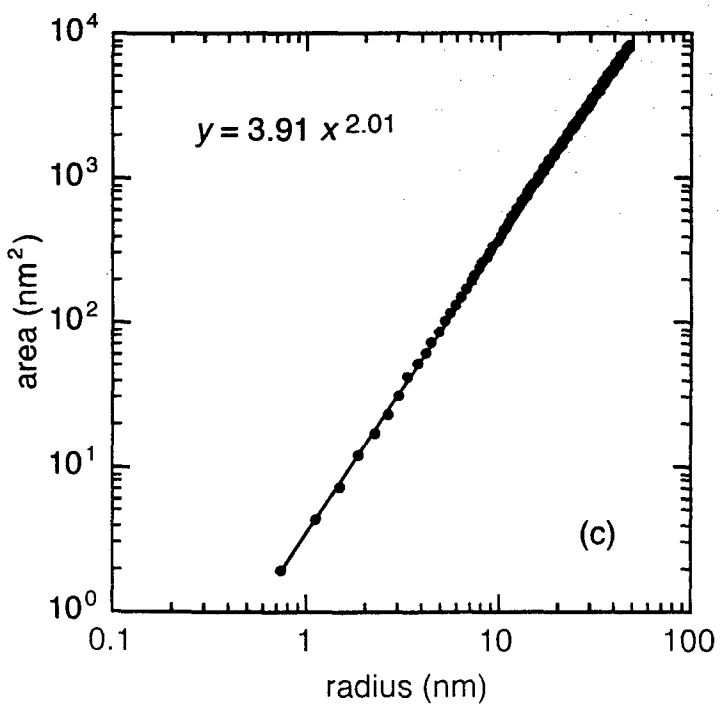
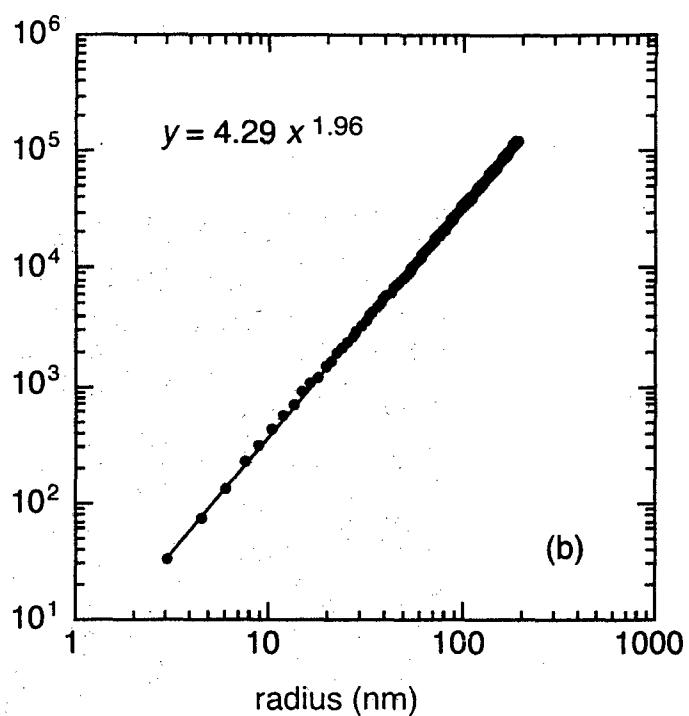
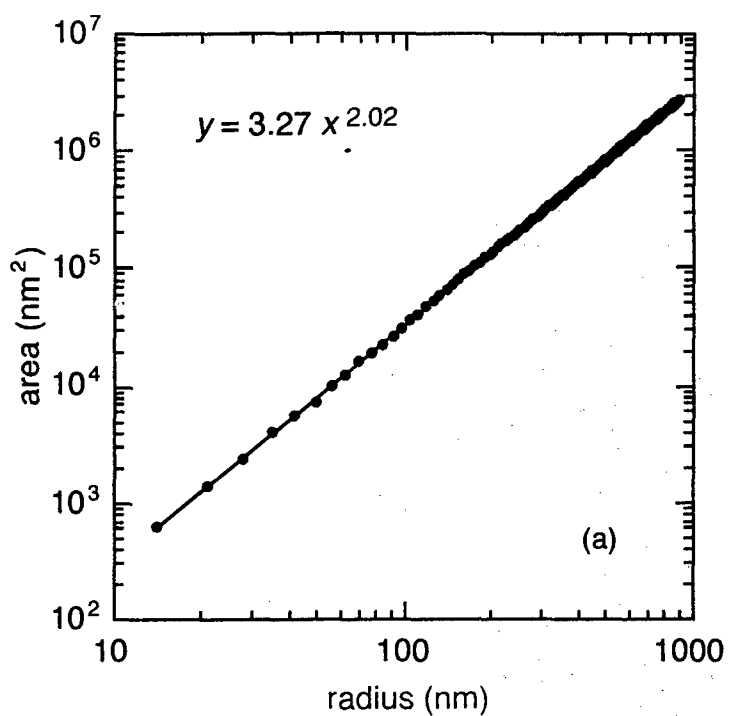
Figure 2 Scanning tunneling microscope images of a thermally oxidized tungsten foil sample. Images (a) through (c) were obtained using a 0.5 V bias applied to the tip and a current set point of 0.5 nA. Image (d) was obtained using a bias voltage of 0.2 V and a current set-point of 0.5 nA. Image (a) was obtained from a typical 1.8  $\mu\text{m}$  square region of the sample and has a RMS corrugation of 60 nm; image (b) was obtained from a 380 nm square near the center of image (a) and has a RMS corrugation of 16 nm; image (c) was obtained from a 95 nm square region near the center of image (b) and has a RMS corrugation of 10 nm; image (d) was obtained from a 17 nm square region near the center of image (c) and has a RMS corrugation of 1 nm. Images were false-shaded to enhance surface detail.

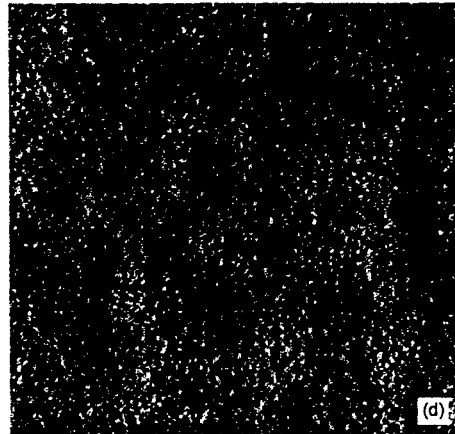
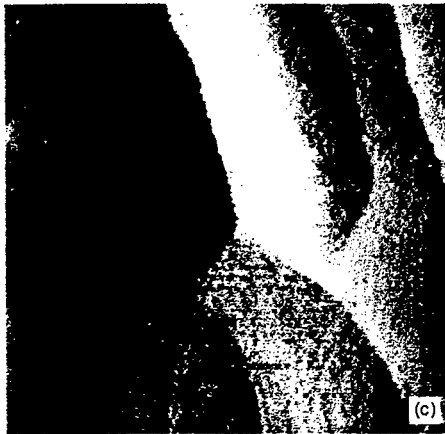
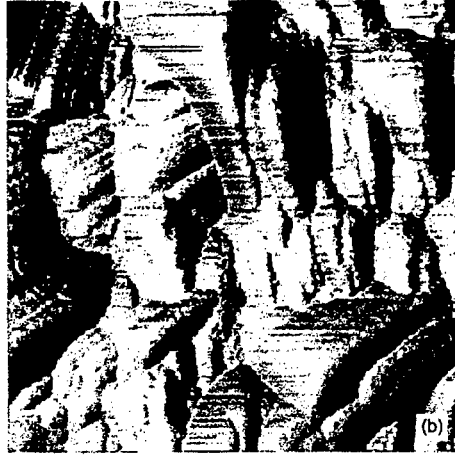
Figure 3 Surface calculated from topographic data as a function of radius of region (see text for explanation). Data plotted in graphs (a) through (d) were obtained from STM images shown in Figure 2(a) through (d) respectively. Line through the data points is a least squares fit. The equation for each line is inset in the graphs with the ordinate representing the surface area and the abscissa representing the radius.

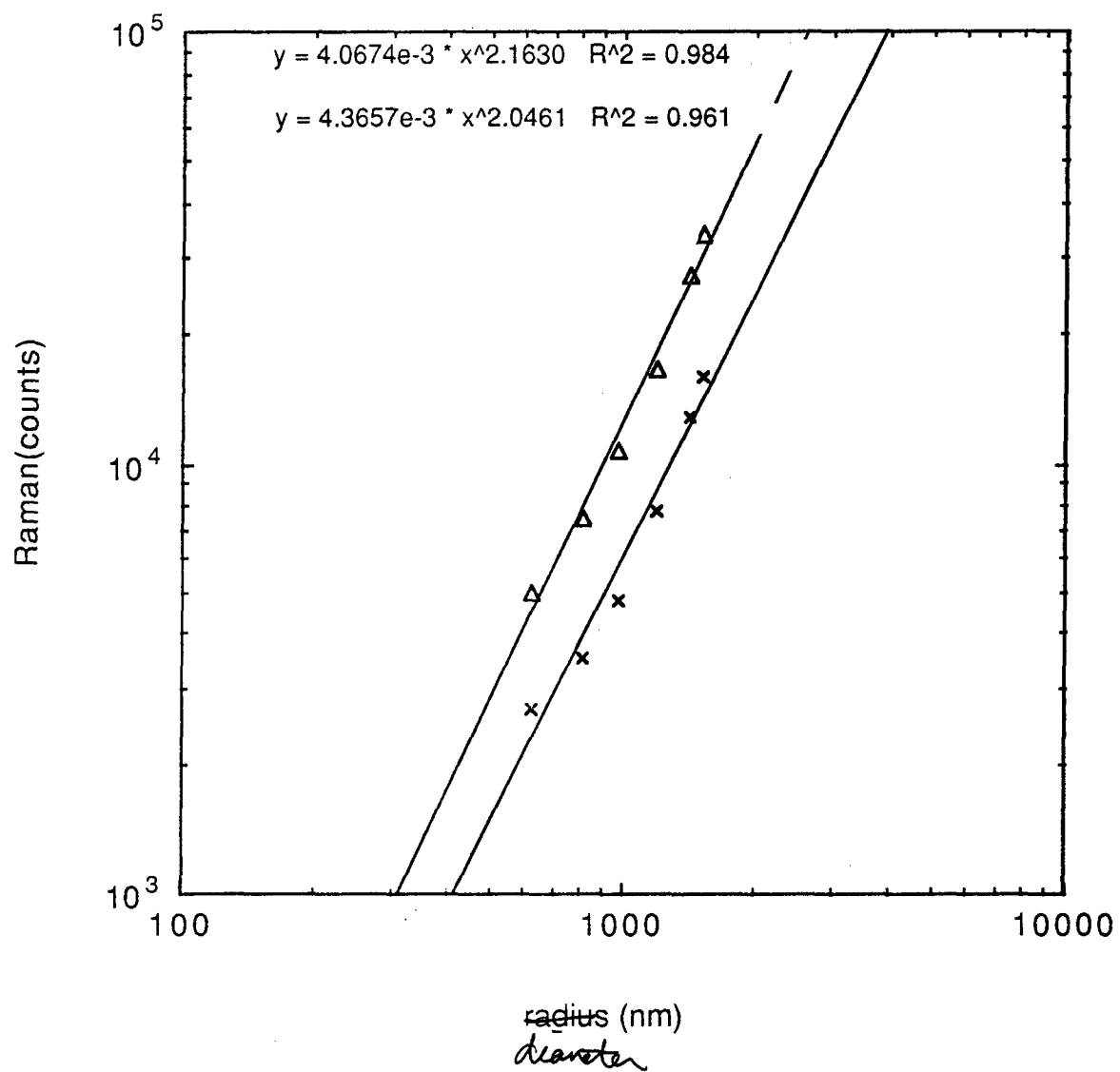
## References

- 1 S. K. Deb, Appl. Opt. 801 (1972), Philos. Mag. 27, 801 (1973)
- 2 Joseph M. Osman, Rebecca J. Bussjager, Fazio Nash, R. M. Villarica, J. Chaiken, Appl. Phys. A. in press
- 3 R. M. Villarica, Fazio Nash, Joseph M. Osman, Rebecca J. Bussjager, J. Chaiken, Proc. Mat. Res. Soc. 397, 347(1996)
- 4 C. G. Granquist, "Handbook of Inorganic Electrochromic Materials", (Elsevier, Amsterdam, 1995)
- 5 M. F. Daniel, B. Desbat and J. C. Lassegues, J. Solid State Chem. 73, 127-139(1988), J. Solid State Chem. 67, 235-247(1987)
- 6 M. Sundberg, R. J. D. Tilley, J. Solid State Chem. 11, 150-160(1974)
- 7 A. N. Kolmogorov, Izv. Akad. Nauk SSSR, Ser. Matem No. 3, 355-359(1937)
- 8 W. Johnson and R. F. Mehl, TAIME 135, 416-442, Discussion 442-458(1939); unpublished details of the derivations in Appendices A-E deposited as ADI number 1182 with the American Society for Information Science (ISIS), 8720 Georgia Avenue, Silver Spring, MD 20910-3603.
- 9 Melvin Avrami, J. Chem. Phys. 7, 1103-1112(1939), J. Chem. Phys. 8, 212-224( 1940), J. Chem. Phys. 9, 177-184( 1941 )
- 10 F. H. Jones, K. Rawlings, J. S. Foord, R. G. Egdell, J. B. Pethica, B. M. R. Wanklyn, S. C. Parker, P. M. Oliver, Surf. Sci. 359, 107-121 ( 1996)
- 11 F. H. Jones, K. Rawlings, J. S. Foord, P. A. Cox, R. G. Egdell, J. B. Pethica, B. M. R. Wanklyn, Phys. Rev. B. 52, R14 392-R14 395(1995-II)
- 12 F. H. Jones, R. A. Dixon, A. Brown, Surf. Sci. 369, 343-350( 1996)
- 13 PZT-SH piezoelectric tubes were purchased from Valpey-Fisher, Inc., Hopkinton, MA
- 14 concentric horizontally oriented tube design first described by J. W. Lyding, S. Skala, J. S. Hubacek, R. Brockenbrough, and G. Gammie, Rev. Sci. Instrum. 59,1897( 1988)
- 15 G. Binnig and D. P. E. Smith, Rev. Sci. Instrum. 57, 1688(1986)

- 16 "stick-slip", or "inertial drive", translator first described by D. W. Pohl, Rev. Sci. Instrum. **58**, 54(1987)
- 17 National Instruments, Inc. Austin, TX
- 18 Aster, Inc., Montagnole, France
- 19 for example see E. Iguchi and R. J. D. Tilley, J. Chem. Phys. **21**, 49- 56( 1977)









# DISTRIBUTION LIST

addresses	number of copies
AIR FORCE RESEARCH LABORATORY/SNDP JOSEPH OSMAN 26 ELECTRONIC PKY ROME NY 13441-4515	10
ATTN: CHIEF SCIENTIST AFRL/IF 26 ELECTRONIC PKY ROME NY 13441-4514	1
AFRL/IFDIL TECHNICAL LIBRARY 26 ELECTRONIC PKY ROME NY 13441-4514	1
ATTENTION: DTIC-OCC DEFENSE TECHNICAL INFO CENTER 8725 JOHN J. KINGMAN ROAD, STE 0944 FT. BELVOIR, VA 22060-6218	2
BALLISTIC MISSILE DEFENSE ORGANIZATION 7100 DEFENSE PENTAGON WASH DC 20301-7100	2
AFRL/IFDIP 26 ELECTRONIC PKY ROME NY 13441-4514	1
RELIABILITY ANALYSIS CENTER 201 MILL ST. ROME NY 13440-8200	1
ATTN: GWEN NGUYEN GIDEP P.O. BOX 8000 CORDNA CA 91718-8000	1

AFIT ACADEMIC LIBRARY/LDEE 1  
2950 P STREET  
AREA B, BLDG 642  
WRIGHT-PATTERSON AFB OH 45433-7765

WRIGHT LABORATORY/MTM, BLDG 653 1  
2977 P STREET, STE 6  
WRIGHT-PATTERSON AFB OH 45433-7739

ATTN: TECHNICAL DOCUMENTS CENTER 1  
DL AL HSC/HRG  
2698 G STREET  
WRIGHT-PATTERSON AFB OH 45433-7604

US ARMY SSDC 1  
P.O. BOX 1500  
ATTN: CSSD-IM-PA  
HUNTSVILLE AL 35807-3801

NAVAL AIR WARFARE CENTER 1  
WEAPONS DIVISION  
CODE 4BL000D  
1 ADMINISTRATION CIRCLE  
CHINA LAKE CA 93555-6100

SPACE & NAVAL WARFARE SYSTEMS CMD 2  
ATTN: PMW163-1 (R. SKIANO) RM 1044A  
53560 HULL ST.  
SAN DIEGO, CA 92152-5002

SPACE & NAVAL WARFARE SYSTEMS 1  
COMMAND, EXECUTIVE DIRECTOR (PD13A)  
ATTN: MR. CARL ANDRIANI  
2451 CRYSTAL DRIVE  
ARLINGTON VA 22245-5200

COMMANDER, SPACE & NAVAL WARFARE 1  
SYSTEMS COMMAND (CODE 32)  
2451 CRYSTAL DRIVE  
ARLINGTON VA 22245-5200

CDR, US ARMY MISSILE COMMAND 2  
REDSTONE SCIENTIFIC INFORMATION CTR  
ATTN: AMSMI-RD-CS-R, DDCS  
REDSTONE ARSENAL AL 35898-5241

ADVISORY GROUP ON ELECTRON DEVICES  
SUITE 500  
1745 JEFFERSON DAVIS HIGHWAY  
ARLINGTON VA 22202

1

REPORT COLLECTION, CIC-14  
MS P364  
LOS ALAMOS NATIONAL LABORATORY  
LOS ALAMOS NM 87545

1

AEDC LIBRARY  
TECHNICAL REPORTS FILE  
100 KINDEL DRIVE, SUITE C211  
ARNOLD AFB TN 37389-3211

1

COMMANDER  
USAISC  
ASHC-IMD-L, BLDG 61801  
FT HUACHUCA AZ 85613-5000

1

US DEPT OF TRANSPORTATION LIBRARY  
FB10A, M-457, RM 930  
800 INDEPENDENCE AVE, SW  
WASH DC 22591

1

AWS TECHNICAL LIBRARY  
859 BUCHANAN STREET, RM. 427  
SCOTT AFB IL 62225-5118

1

AFIWC/MSY  
102 HALL BLVD, STE 315  
SAN ANTONIO TX 78243-7016

1

SOFTWARE ENGINEERING INSTITUTE  
CARNEGIE MELLON UNIVERSITY  
4500 FIFTH AVENUE  
PITTSBURGH PA 15213

1

NSA/CSS  
K1  
FT MEADE MD 20755-6000

1

ATTN: OM CHAUDHAN  
DCMC WICHITA  
271 WEST THIRD STREET NORTH  
SUITE 6000  
WICHITA KS 67202-1212

1

AFRL/VSDS-TL (LIBRARY)  
5 WRIGHT STREET  
HANSCOM AFB MA 01731-3004

1

ATTN: EILEEN LADUKE/D460  
MITRE CORPORATION  
202 BURLINGTON RD  
BEDFORD MA 01730

1

BUSO(P)/DTSA/DUTD  
ATTN: PATRICK G. SULLIVAN, JR.  
400 ARMY NAVY DRIVE  
SUITE 300  
ARLINGTON VA 22202

2

RICHARD PAYNE  
AIR FORCE RESEARCH LAB/SNH  
HANSCOM AFB, MA 01731-5000

1

JOSEPH P. LORENZO, JR.  
AIR FORCE RESEARCH LAB/SNHC  
HANSCOM AFB, MA 01731-5000

1

JOSEPH L. HORNER  
AIR FORCE RESEARCH LAB/SNHC  
HANSCOM AFB, MA 01731-5000

1

RICHARD A. SOREF  
AIR FORCE RESEARCH LAB/SNHC  
HANSCOM AFB, MA 01731-5000

1

JOHN J. LARKIN  
AIR FORCE RESEARCH LAB/SNHX  
HANSCOM AFB, MA 01731-5000

1

ALBERT A. JAMBERDINO  
AIR FORCE RESEARCH LAB/IFED  
32 HANGAR RD  
ROME NY 13441-4114

1

AIR FORCE RESEARCH LAB/SND  
25 ELECTRONIC PKY  
ROME NY 13441-4515

1

JOANNE L. ROSSI  
AIR FORCE RESEARCH LAB/SNW  
25 ELECTRONIC PKY  
ROME NY 13441-4515

1

NY PHOTONIC DEVELOPMENT CORP  
MVCC ROME CAMPUS  
UPPER FLOYD AVE  
ROME, NY 13440

1

ROBERT T. KEMERLEY  
AIR FORCE RESEARCH LABORATORY/SND  
2241 AVIONICS CIRCLE, RM C2G69  
WRIGHT-PATTERSON AFB OH 45433-7322

1